THESIS FOR THE DEGREE OF DOCTOR OF PHILOSOPHY

From experiments with images to 3D models

Henrike Häbel

Division of Applied Mathematics and Statistics
Department of Mathematical Sciences
Chalmers University of Technology and University of Gothenburg
Göteborg, Sweden 2017

This work is part of the VINN Excellence Centre SuMo Biomaterials and is supported by the Swedish Governmental Agency for Innovations Systems, VINNOVA, the Knut and Alice Wallenberg Foundation, KAW, and the Swedish Foundation for Strategic Research, SSF.

From experiments with images to 3D models
Henrike Häbel
Göteborg 2017
ISBN: 978-91-7597-569-6

Doktorsavhandlingar vid Chalmers tekniska högskola
Ny serie nr 4250
ISSN 0346-718X

Department of Mathematical Sciences
Chalmers University of Technology and University of Gothenburg
SE-412 96 Göteborg, Sweden
Phone: +46 (0)31 772 8296
Author e-mail: henrike.habel@chalmers.se

Cover:
A scanning transmission electron microscopy image of a silica nanoparticle gel (top), a scanning electron microscopy image of the cross-section of an ethyl cellulose containing porous film (bottom) and a schematic visualization of three-dimensional models of particles and pores.

Typeset with LaTeX.
Department of Mathematical Sciences
Printed in Göteborg, Sweden 2017

From experiments with images to 3D models

Henrike Häbel

Department of Mathematical Sciences
Chalmers University of Technology and University of Gothenburg

Abstract

For developing the next generation sustainable materials, it is often crucial to understand and control their properties and function. This work presents cross-disciplinary research starting with experimentally fabricated porous soft biomaterials and images of their micro-structure obtained by electron or laser microscopy. It is investigated how much information on the three-dimensional material structure can be extracted from two-dimensional images and how conclusions compare to three-dimensional image analysis. Based on the image data, spatial statistical models are constructed and fitted to two different materials: a colloidal nanoparticle gel and a porous polymer blended film. Colloidal systems are everywhere in our everyday life and of high interest for the development of new advanced materials. Polymer films are popular for pharmaceutical coatings which control the release of a drug to obtain important therapeutic benefits.

Besides presenting image analysis routines, three-dimensional finite Gibbs point processes with inhomogeneous and anisotropic pair-potential functions are introduced. Observed point patterns are formed by silica particle positions or pore branching points located at intersections of at least three pore channels. Due to physical chemical forces between particles and polymers, it is assumed that the points interact with each other. The pairwise interaction is described in the pair-potential function of a Gibbs process. In this way, there is a link between static Gibbs point process models and dynamic physical chemical processes like colloidal particle aggregation and polymer phase separation. Furthermore, a new spatial statistical summary function is suggested for the cluster size analysis on different length scales in aggregated structures. This function is a useful tool for comparing two regimes for particle aggregation resulting in different size and shape distributions of particle clusters. More precisely, it is used to study the diffusion limited and the reaction limited cluster aggregation.

The methods introduced in this work can be applied to point processes in general and are important contributions to the point process literature. The results are useful for setting up a virtual design framework for the study of properties of various materials, which may not yet have even been synthesized, in simulation studies instead of experiments involving valuable resources.

Keywords: Anisotropy, colloidal particle aggregation, Gibbs point processes, image analysis, mass transport, porous polymer blended films.

List of appended papers

Paper I Nordin, M., Abrahamsson, C., Hamngren Blomqvist, C., **Häbel, H.**, Röding, M., Olsson, E., Nydén, and M., Rudemo, M. (2014). Estimation of mass thickness response of embedded aggregated silica nanospheres from high angle annular dark-field scanning transmission electron micrographs. *Journal of Microscopy*, 253 (2):166-170. doi:10.1111/jmi.12107.

Paper II **Häbel, H.**, Särkkä, A., Rudemo, M., Hamngren Blomqvist, C., Olsson, E., Abrahamsson, C., and Nordin, M. (2016). From static micrographs to particle aggregation dynamics in three dimensions. *Journal of Microscopy*, 262 (1):102-11. doi:10.1111/jmi.12349.

Paper III **Häbel, H.**, Särkkä, A., Rudemo, M., Hamngren Blomqvist, C., Olsson, E., and Nordin, M. (2017). Colloidal particle aggregation in three dimensions. *In manuscript*.

Paper IV **Häbel, H.**, Andersson, H., Olsson, A., Olsson, E., Larsson, A., and Särkkä, A. (2016). Characterization of pore structure of polymer blended films used for controlled drug release. *Journal of Controlled Release*, 222: 151-158. doi: 10.1016/j.jconrel.2015.12.011.

Paper V **Häbel, H.**, Rajala, T., Boissier, C., Marucci, M., Schladitz, K., Redenbach, C., and Särkkä, A. (2017). A three-dimensional anisotropic point process characterization for pharmaceutical coatings. *Submitted*.

My contribution to the appended papers:

Paper I: I validated the developed log-likelihood method for the estimation of mass thickness response in a simulation study.

Paper II: I co-developed the particle detection algorithm, developed a new summary function for cluster size and conducted all statistical analyses. I did most of the writing of the publication.

Paper III: I extended the new summary function for cluster size to three dimensions, conducted all statistical analyses and implemented a method for estimating the probability of aggregation based on the pair-potential function. I did most of the programming of new R functions for 3D Gibbs processes and writing of the publication.

Paper IV: I co-developed a routine for the polymer phase segmentation of cross-sections, conducted all statistical analyses and did most of the writing of the publication.

Paper V: I was involved in the experimental film preparation, co-developed a routine for the polymer phase image analysis and conducted all statistical analyses. I constructed new anisotropic pair-potential functions, did most of the programming of new R functions for inhomogeneous and anisotropic 3D Gibbs processes and writing of the publication.

Publications not included in this thesis:

Hamngren Blomqvist, C., Gebäck, T., **Häbel, H.**, Altskär, A., Hermansson, A.M., Gustafsson, S., Lorén, N., and Olsson, E. (2017). Three-dimensional analysis of nanoscale pore-morphology and simulated mass transport in particulate silica hydrogels. *In manuscript*.

Andersson, H., **Häbel, H.**, Olsson, A., Olsson, S., von Corswant, C., Hjärtstam J., Persson M., Stading M., and Larsson, A. (2016). Modification of structure and mass transport in phase separated films for controlled release varying the molecular weight of the water-soluble polymer. *International Journal of Pharmaceutics*, 511 (1):223-235. doi:10.1016/j.ijpharm.2016.06.058.

Karimi, M., Hedner, J., **Häbel, H.**, Nerman, O., and Grote, L. (2016). A sleep apnea related excess risk of motor vehicle accidents in the Swedish Traffic Accident Registry is reduced by CPAP - a retrospective cohort study. *Sleep*, 38 (3), 341-349. doi:10.5665/sleep.4486.

In all chaos there is a cosmos,
in all disorder a secret order.

Carl Gustav Jung (1875 - 1961)

Acknowledgments

During my years as a Ph.D. student, I was faced with a chaos of irregularly arranged points, cross-disciplinary research ideas and quite a substantial amount of image data, computer programs and articles. Without my supervisors, I would never have managed to bring everything into order. First of all, I thank **Aila Särkkä** for being the best supervisor I could have wished for. Not only has she been one of the reasons for me to take on the challenge of perusing a Ph.D. degree, but she has also given me the support to develop and follow my own research ideas. I thank **Mats Rudemo** for always being there when needed and all valuable comments. I thank **Tuomas Rajala** for teaching me how to improve my coding in R and trying to introduce a better order to them. Last, but not least, I thank **Matias Nordin** for showing me more of the world of physics in Gothenburg and California.

I am very thankful for a great collaboration with **Mariagrazia Marucci** and **Catherine Boissier** at AstraZeneca R&D Mölndal - I am happy that I did not blow up the laboratory - and with **Claudia Redenbach** and **Katja Schladitz** in Kaiserslautern. Furthermore, I thank **Christoffer Abrahamsson, Helene Andersson, Charlotte Hamngren Blomqvist, Anna Olsson**, and **Eva Olsson** for exciting cross-disciplinary research, which brought forth articles as well as friendship.

I am grateful for the inspiriting cross-disciplinary research group created within SuMo Biomaterials and the SSF/KAW project group. I have always enjoyed the fruitful discussions with **Christian von Corswant, Cecilia Fager, Tobias Gebäck, Charlotta Hanson, Alexey Heintz, Mats Josefson, Anette Larsson, Niklas Lorén**, and **Holger Rootzén**. I also thank **Emilio Porcu** and **Orietta Nicolis** for welcoming me in Valparaíso.

"Within-disciplinary" seminars, conferences and summer schools would not be as interesting and fun if it was not for **Anders, Anna-Kaisa, Christophe, Claes, David, Farzaneh, Pratheepa, Jonas, Marco, Ottmar**, and **Sandra**. I would not have enjoyed my work and life in Sweden without **Anna J., Hossein, Johan, John, Jonatan, Malin, Roza, Sebastian, Tobias Ö., Valentina**, and many more. Thank you for getting me into the pool, **Alexey**, onto the bike **Dawan, Magnus Ö.**, and **Peter**, and up the wall, **Anton** and **Jules**. I said that I cannot have lived in Sweden without having tried Innebandy. Thanks to **Ivar, Matteo, Maud, Olle**, and **Timo** it became a special experience. Thank you, **Fredrik, José, Magnus R., Robert**, and **Viktor** for great evenings and travels. Thank you, **Barbara** and **Pia** for staying so good in touch and the lovely frequent visits.

The last words here, I would like to devote to those who have accompanied me through my life and helped me to grow as a person. Starting chronologically, I am really thankful for **Lea, Kirsten**, and **Sandra** for a quarter-of-a-century long friendship beyond boarders and babies. I thank **Kristin** for a decade in good and bad times, where we learned from and with each other. Starting from the beginning of our Ph.D. studies five years ago, I am grateful that **Mariana** was there to listen, laugh, and cry.

A special thanks goes to **Richard** for all understanding, love, and support during the crucial months of my last Ph.D. year.

I would like to thank my family for understanding that I cannot make it to every family gathering even though I would love to. Of course, the biggest word of thank goes to my parents, **Sabine** and **Roland**, who may sometimes have tried to control my chaos a little too much, but have always supported me in following my dreams. I love you!

Henrike Häbel
Gothenburg, April 29, 2017

This thesis is dedicated to my parents.
Mit Dank für Liebe, Unterstützung und Flügel.

Important abbreviations

CLSM	confocal laser scanning microscopy
CSR	completely spatially random
DLCA	diffusion limited cluster aggregation
DLVO	Derjaguin-Landau-Vervey-Overbeek (theory)
EC	ethyl cellulose
HAADF	high-angular annular dark field
HPC	hydroxypropyl cellulose
M_w	molecular weight
RLCA	reaction limited cluster aggregation
SEM	scanning electron microscopy
STEM	scanning transmission electron microscopy
%wt	percent weight
w/w	weight/weight
2D	two-dimensional/dimensions
3D	three-dimensional/dimensions

Contents

1 Introduction **1**
- 1.1 Historical perspective . . . 3
- 1.2 Aims . . . 4

2 Physical and chemical methodology **5**
- 2.1 Brownian motion and diffusion . . . 5
- 2.2 Colloidal particle aggregation . . . 6
- 2.3 Polymer phase separation . . . 8
- 2.4 Electron and confocal laser scanning microscopy . . . 9

3 Materials **11**
- 3.1 Colloidal nanoparticle gels . . . 11
- 3.2 Polymer blended films . . . 12

4 Image analysis **13**
- 4.1 Image filtering and segmentation . . . 13
- 4.2 Morphological operations . . . 14
- 4.3 Particle detection . . . 15

5 Spatial point processes **17**
- 5.1 Basic definitions . . . 17
- 5.2 Functional summary characteristics . . . 19
  - 5.2.1 Distance distribution functions . . . 20
  - 5.2.2 Second-order characteristics . . . 21
  - 5.2.3 Third-order characteristic . . . 22
  - 5.2.4 Mean cluster size function . . . 22
- 5.3 Finite pairwise interaction Gibbs processes . . . 24

6 Summary of appended papers **29**
- 6.1 Paper I-III: Colloidal nanoparticle gels . . . 29
- 6.2 Paper IV and V: Polymer blended films . . . 34

7 Conclusions **37**

1 Introduction

An increasing global demand for resources, energy and waste recovery has resulted in a great need for new sustainable materials. The presented research is a contribution to the development of the next generation biomaterials by using predictive science with a reduced number of experiments based on valuable resources. In this work, porous biomaterials are of special interest. We investigate how the material formation affects the final pore structure and mass transport properties, which are important for the function of the material. The relationship between mass transport and the function of a material is of great importance in various everyday life applications ranging from clothes (Wang and Sun, 2014) and personal hygiene products (Yadav et al., 2016) to the storage of charges in batteries and solar cells (Nordström et al., 2010; Yuan et al., 2011). Here, we study two porous materials: a colloidal particle gel, which can serve to fabricate test beds for mass transport, and a polymer blended film for oral controlled drug release formulations (Qui and Zhang, 2000).

The pore structure in a colloidal particle gel is determined by the final particle network formed during an aggregation process. That is why it is of interest to understand and control the aggregation dynamics in order to obtain, maintain, or predict specific structures. Milk is probably the most known colloid and the making of cheese a good example for the relevance of obtaining desired structures (Evans and Wennerström, 1994; de Kruif et al., 1995). In biological fluids like blood, it is important to maintain the stability of the system, and prediction of aggregation is crucial for treating protein aggregation-related neurodegenerative diseases (Giacomelli et al., 2017), for instance.

Porous polymer blended films are popular for oral controlled release formulations, where the pore structure can be tuned for delayed, sustained, and repeated drug release (Wen and Li, 2010). Polymers are formed by molecules featuring repetitions of consecutive units called monomers. There are many different kinds and groups of polymers, but especially bio-based polymers produced from renewable resources have gained global importance (Klemm et al., 2005). The films studied here are blends of two cellulosic polymers, which are non-toxic, non-allergenic, and have good film forming properties and stability (Marucci et al., 2009; Siepmann et al., 2008). There are several factors relevant for the film formation and it is important to understand how desired properties of the final pore structure can be achieved. Among these properties, pore tortuosity and connectivity are of special interest, since they directly affect the overall releasability of the drug (Siegel, 2012).

All research presented in this thesis starts with experiments to prepare, analyse and image the material. In order to complement the experimental analysis, the pore structure of materials is characterized and modeled using image analysis and tools from spatial statistics. Even though three-dimensional (3D) images are a natural choice for studies on 3D structures, two-dimensional (2D) images are often easier and faster obtained. Both 2D and 3D images are processed to extract objects of interest like silica particle positions or locations of pore branching points. A set of extracted locations forms a point pattern which is mathematically expressed as a realization of a spatial point process. For the study of point processes, spatial statistical summary functions are often used to describe and characterize the spatial arrangement of the points. The obtained information is used to construct and fit models based on spatial Gibbs point processes. A point process model can be of great use for characterizing given data. Even the model construction in itself may reflect some aspects of the material formation. Furthermore, fitted models can be used to virtually design structures and to investigate on how structural changes affect mass transport properties. Once desired properties of the material are determined, further experiments can be used to verify results of the simulation study. Figure 1.1 summarizes the workflow from experiments with images to 3D models.

Figure 1.1: Workflow from experiments with images to 3D models: Materials are experimentally prepared and imaged using electron or laser microscopy. The images are processed in an image analysis routine and methods from spatial statistics are used to characterize and model the material structure. Conclusions drawn from the model can provide valuable input for further experiments.

The following subsections, 1.1 *Historical perspective* and 1.2 *Aims*, give a historical background to the underlying physics, chemistry and mathematics and present the aims of this thesis in a cross-disciplinary context. An introduction to important concepts on aggregation and polymer phase separation is given in Section 2 *Physical and chemical methodology*. Furthermore, the microscopy techniques used for 2D and 3D imaging are briefly described. Information on the material preparation and imaging is given in Section 3 *Materials*. The applied methods from image analysis and spatial statistics are introduced in Section 4 *Image analysis* and Section 5 *Spatial point processes*, respectively. Finally, the papers appended to this thesis are presented by summarizing their main results and conclusions in Section 6 *Summary of appended papers*. Section 7 *Conclusions* ends with general conclusions on how results from this work can be useful for future research.

1.1 Historical perspective

This work addresses colloidal particle aggregation and polymer phase separation. Both phenomena are driven by electrostatic interactions and theories on their kinetics have been developed in statistical mechanics. Whereas in older fields such as thermodynamics, a particular system is followed through its succession of configurations, the goal in statistical mechanics is to determine the distribution of all possible configurations. A good example is the Ising model initially intended as a model for magnetic systems with two discrete spin states. The energy at each site depends on the states in a small neighborhood, where a pair of different spin states has an interaction energy. Statistical mechanics can be used to determine the most probable configuration and solve for the thermodynamic variables (Evans and Wennerström, 1994, p.446).

Statistical mechanics had its start in the second half of the nineteenth century, when van der Waals, Boltzmann, Maxwell and Gibbs were the first to unify thermodynamic and probabilistic concepts for intermolecular forces. One of these concepts is the Gibbs distribution, which describes the equilibrium states of subsystems of systems with a very large number of particles (Gibbs, 1902; Israelachvili, 2011; Chiu et al., 2013).

The Gibbs measure was first discussed in statistical mechanics by Ruelle (1969, p.137) and became an inspiration to a new class of point processes. Point process theory had been developed in the first half of the twentieth century motivated by research problems in physics, biology and queuing theory related to random patterns observed on different scales ranging from trees in a forest to nanosized particles. In the nineteen seventies during the development of the modern phase of the theory (Chiu et al., 2013, p.108), Gibbs point processes were introduced in spatial statistics. Among all pioneer work on Gibbs point processes, sometimes also called Markov point processes, Ripley and Kelly (1977) probably became the most significant. Both the Gibbs measure and a Gibbs point process are useful frameworks for studying pairwise interaction, which can be described by a pair-potential function. From the physical perspective, the potential is the result of electrostatic repulsive and attractive forces. In a similar fashion, attraction and repulsion between points is captured by Gibbs point processes. A physicist or chemist usually chooses a potential and studies the resulting structures, whereas a spatial statistician is interested in estimating the underlying pair-potential function from an observed point pattern.

Current microscopy techniques provide more information of micro-, meso- and nanostructures of systems or materials on a scale of a thousandth of a millimeter or even smaller on the molecular-scale. Obtained images enable a characterization of structures and open up opportunities to understand and control material properties and functions by manipulating the operative forces. The focus has shifted from simple atoms and molecules in gases to colloidal systems, liquid structures and thin films. Soft matter, self-assembling systems and smart materials are some examples of recent hot topics. The interest became so broad that it gave rise to many cross-disciplinary collaborations and this work is one of them.

1.2 Aims

Spatial statistical analyses of pore structures can provide quantitative information valuable for understanding and controlling mass transport properties and function of a material. The aim of my work is to characterize and model the structure of two different porous materials, but the developed methods and models can be used in point pattern analyses in general. Four main objectives are encountered while developing feasible methods and constructing suitable models.

- Develop feasible image analysis routines to extract important material characteristics from microscopy images (**Paper I-V**).
- Explore how much information on a 3D structure can be obtained from 2D images (**Paper I-V**).
- Explain physical chemical dynamics with static images and models (**Paper II, III, V**).
- Characterize and model inhomogeneous and anisotropic structures with a simple and efficient methodology that can be applicable to various materials (**Paper V**).

2 Physical and chemical methodology

2.1 Brownian motion and diffusion

Brownian motion is one of the most important concepts in many applications involving random molecular motion of particles, macromolecules or aggregates in liquids. The corresponding mathematical model for a Brownian particle or object in $\mathbb{R}^d$ is described by a Wiener process which is a time-continuous stochastic process

$$\{B(t)\}_{t\geq 0},\ B(t) = (B^1(t), \ldots, B^d(t))$$

with the following properties (Grimmett and Stirzaker, 2001, p. 514 ff.)

B1 $B(0) = \mathbf{0}$,

B2 $B^1, \ldots, B^d$ are independent and identically distributed processes,

B3 $B^i(s+t) - B^i(s) \sim \mathcal{N}(0, \sigma^2 t) \quad \forall i = 1, \ldots, d,\ s, t \geq 0,\ \sigma^2 > 0$,

B4 B^i has independent increments for all $i = 1, \ldots, d$.

In Einstein (1905) a differential equation for the movement of n particles (for $d = 2$) is given by

$$\frac{\partial m}{\partial t} = D\frac{\partial^2 m}{\partial x^2},$$

with solution

$$m(x,t) = \frac{n}{\sqrt{4\pi D t}} \exp\left(-\frac{x^2}{4Dt}\right)$$

where $m(x,t)$ gives the density of particles at time t. Einstein's equation

$$D = \frac{\overline{x^2}}{2t}$$

defines the diffusion coefficient $D > 0$ as a function of distance x that a particle moves in time t, where $\sigma^2 = 2D$ in property B3.

As objects move, they interact with the surrounding liquid molecules. This so-called hydrodynamic interaction has an effect on its diffusion coefficient $D > 0$. Hence, it makes sense to define

$$D = \frac{k_B T}{M\xi}$$

with a friction coefficient $\xi > 0$ for moving objects with mass $M > 0$. The constant $k_B T$ is the thermal energy of the system at room temperature, where $k = 1.38065 \cdot 10^{-23}$J/K is the Boltzmann constant. For uniform spheres with radius $R > 0$, the friction coefficient is given by $\xi = 6\pi\eta R/M$, where η is the solvent viscosity (Deutch and Oppenheim, 1987,Evans and Wennerström, 1994, p.340 f.).

Diffusion is one of two common mass transport properties. The other one is flow which gives the local velocities of objects transported along pressure or gravitational gradients (Cussler, 1997, p.16 ff.).

2.2 Colloidal particle aggregation

A corner stone in colloid science is the Derjaguin-Landau-Vervey-Overbeek (DLVO) theory developed in 1945. It quantitatively describes interaction between two colloidal particles depending on their distance. Attractive van der Waals and electrostatic repulsive forces form the overall interaction potential as a function of inter-particle distance. In a colloidal stable dispersion, the electrostatic repulsion between particles is strong enough to prevent the particles from overcoming a potential barrier and aggregation. The potential barrier can be lowered by changing the pH or by adding salt (NaCl) so that particles start to aggregate (Evans and Wennerström, 1994). Figure 2.1 schematically shows the particle aggregation process. In a stable solution (A), particles move according to Brownian motion in a water-based solution. Upon destabilization, the particles start to aggregate and form clusters (B). The aggregation, also referred to as gelation, is completed when all particles have aggregated into one large cluster (C).

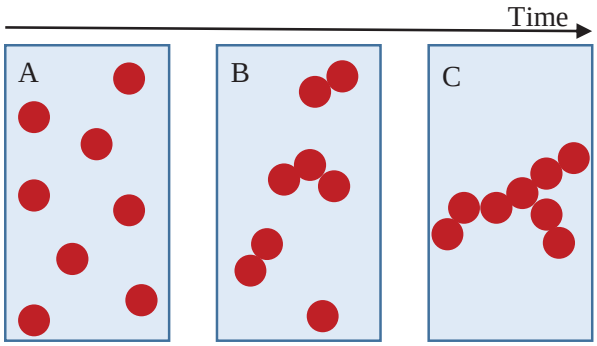

Figure 2.1: Schematic illustration of aggregation of colloidal particles in a stable dispersion (A), forming particle clusters after destabilization (B) and finally a gel (C).

Two common models that describe (irreversible) aggregation dynamics (B in Figure 2.1) of particles or particle clusters are the diffusion limited cluster aggregation (DLCA, (Meakin, 1983)) and the reaction limited cluster aggregation (RLCA, (Kolb and Jullien, 1984)). These two models can be interpreted as different limiting behaviors of colloidal aggregation. In the DLCA case, no repulsive forces act between particles making them aggregate upon collision. Consequently, the limiting behavior affecting the final structure is the diffusion of the particles. For the RLCA process, there are strong repulsive forces between the particles such that many particle collisions may occur before aggregation. The different aggregation dynamics can be described by the probability of aggregation upon collision. It is one in the DLCA and close to zero in the RLCA regime. Figure 2.2 presents one simulation from the DLCA ($p = 1$) and the RLCA ($p = 0.0001$) regime in 3D, corresponding 2D artificial micrographs with detected particles and schematic illustrations of the typical cluster shapes. It can be seen that the particle clusters in the DLCA regime generally branch and spread more than in the RLCA regime, where clusters tend to be tighter.

DLVO, DLCA and RLCA provide simple frameworks for studying colloidal aggregation. However, interaction forces between silica particles are complex, in particular at the small-scale (nm). A full model for the interaction between particles and particle clusters, also needs to include so called entropy effects like hydrodynamic interaction with water molecules (Evans and Wennerström, 1994, p. 231 ff.).

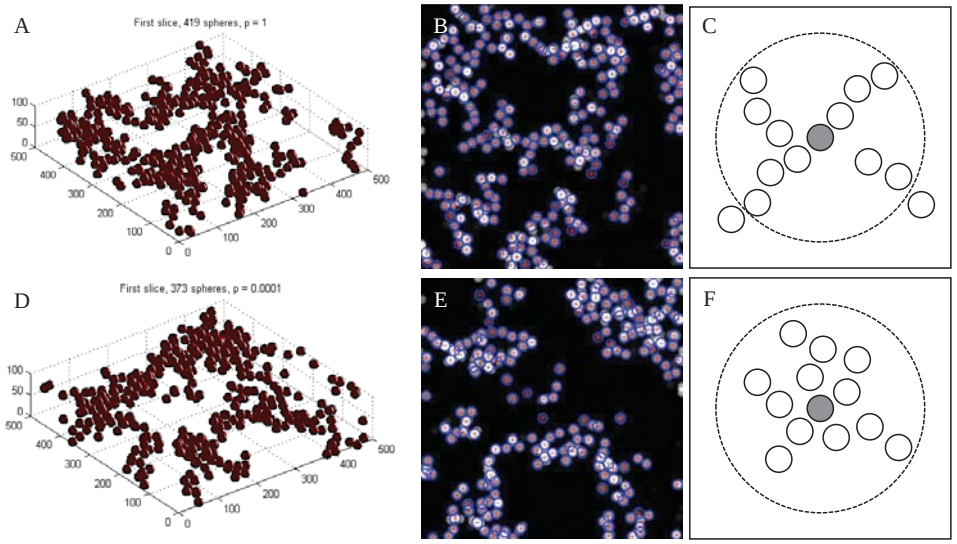

Figure 2.2: Left: example of simulation from the DLCA ($p = 1$, top) and the RLCA ($p = 0.0001$, bottom) process in 3D. Middle: corresponding 2D artificial micrographs. Detected particles are marked by circles and their center location by crosses. Right: schematic illustration of the typical cluster shape around the origin marked in gray within a certain distance indicated by the dashed circles.

2.3 Polymer phase separation

We can observe phase transition and phase separation in our everyday life, when ice melts to water or when water separates from oil. Studying phase behavior provides a link between structure and intermolecular interactions, which is important to understand for controlling the final structure. Even small changes to a system may trigger phase changes resulting in a large diversity of structures. For example, in Section 2.2 it was described how small changes to the pH or the salinity of a silica in water dispersion can lead to various different aggregated structures. This section focuses on phase separation in polymer-polymer-solvent systems.

In a solution with two incompatible polymers with concentrations above a critical value, phase separation can be achieved in several ways, for instance, by solvent evaporation or by changing the temperature. There are several factors affecting the final structure. Examples are polymer contents and viscosity. Viscosity, meaning the polymers resistance to flow, depends on the degree of entanglements of the polymer chains, which in turn depends on the molecular weight of the polymer (Marucci et al., 2013).

The phase separation dynamics are driven by interfacial tension with two distinct mechanisms, nucleation and growth and spinodal decomposition, schematically introduced in Figure 2.3. In both cases, domains grow as the system strives to reach a lower energy by minimizing the surface interfacial area between the phases. Consequently, larger domains form. In nucleation and growth, droplet-like domains appear and grow independently with time. Spinodal decomposition results in periodic domains, which can be droplet-like or continuous, and grow regularly with time (Cowie and Arrighi, 2007; Jones and Richards, 1999).

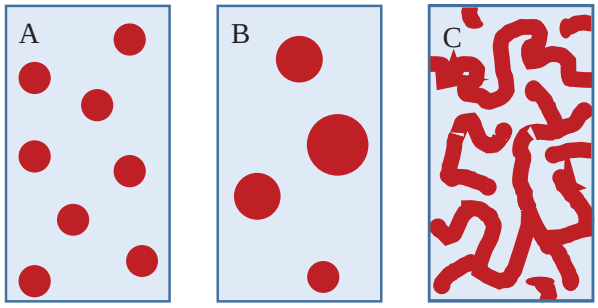

Figure 2.3: Schematic illustration of phase separation of a homogeneously blended solution (A) by nucleation and growth (B) or spinodal decomposition (C).

2.4 Electron and confocal laser scanning microscopy

All image data were obtained by the electron or confocal laser scanning microscopy techniques schematically presented in Figure 2.4. In scanning transmission electron microscopy (STEM), a focused electron beam scans over a sample which has to be sufficiently thin in order to obtain transmission of the electrons. At each position of the beam, electrons are scattered upon interaction with the material. Thus, electrons transmitted through the sample carry information about the microstructure of the material. A high-angle annular dark-field (HAADF) detector collects the electrons which are scattered through high angles. In scanning electron microscopy (SEM), surface topographical contrast is provided by secondary electrons that are knocked out from atoms in the sample by the primary electron beam. The secondary electrons exit the sample at the surface and are collected by a low voltage detector. The primary beam electrons have considerably higher energy than the secondary electrons and hence are not significantly affected by the relatively low voltage bias of the detector (Pennycook et al., 2006).

Two different imaging techniques were applied to obtain 3D images. The first technique, STEM tomography, is based on a tilt series of STEM images collecting data from different angles. The angular interval and other relevant settings should be carefully chosen such that a sufficiently large number of high quality images is obtained. A 3D reconstruction of the sample is constructed by aligning the images (Hawkes, 2006). Instead of an electron beam, the second technique is based on laser light. In confocal laser scanning microscopy (CLSM), the laser is focused onto a pinhole and directed to a small volume inside a fluorescing sample. If there is no natural fluorescence in the sample, a fluorescent dye can be used to label the material. Fluorescent light is emitted and collected by a photon detector. Different depth of the sample can be reached by changing the confocal length (Stelzer, 1990).

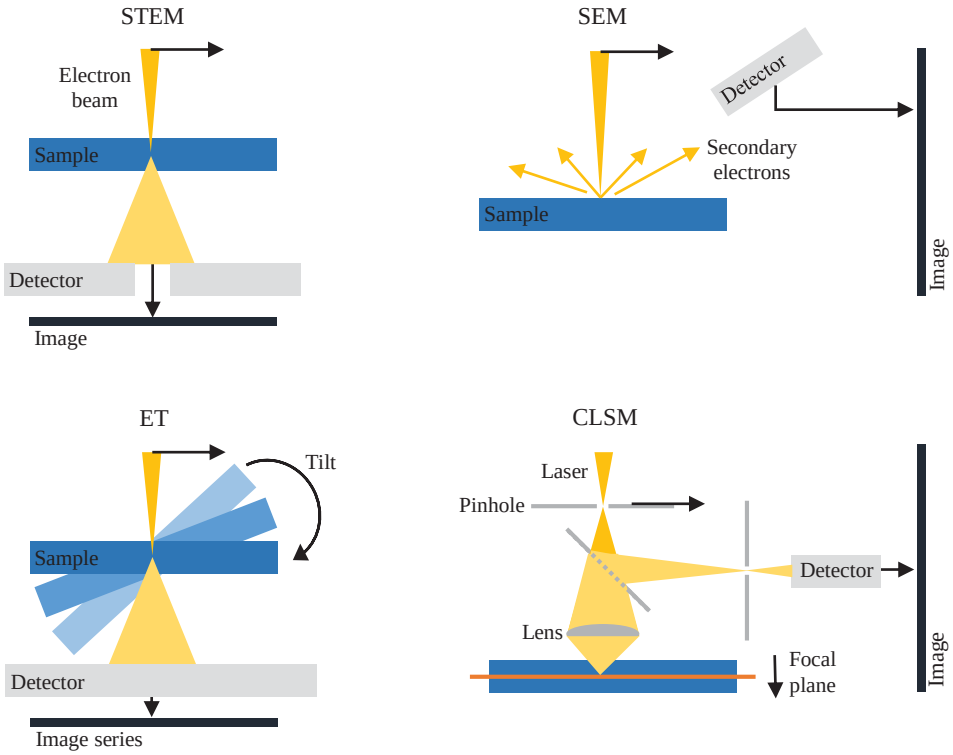

Figure 2.4: Schematic illustration of 2D imaging by scanning transmission electron microscopy (STEM) or scanning electron microscopy (SEM) and 3D imaging by electron tomography (ET) or confocal laser scanning microscopy (CLSM).

3 Materials

3.1 Colloidal nanoparticle gels

In Paper I-III, we study the irreversible aggregation of colloidal silica nanoparticles as they offer a broad variety of different structures with well known gelation properties. The diameter of a particle was assumed to be approximately 20 nm with values ranging from about 18 to 33 nm. Gels at 9 %wt, which corresponds to a 5.96% silica volume fraction, were formed from a water-based silica dispersion. During the gel fabrication, the pH level was lowered from 9.1-9.2 to 7.8 by ion exchange. The dispersion was filtered, ultra-pure deionized water with 0.5 M NaCI (aq) was added, and the mixture was left to gel for 14 days.

2D and 3D images were obtained by HAADF-STEM (tomography) of small gel samples. Each gel sample needed to be prepared for the high-vacuum condition in electron microscopy by carefully replacing the water within the gel by a resin. The infiltrated samples were embedded in plastic and cut in an ultramicrotome with a diamond knife to obtain thin sections appropriate for STEM. Figure 3.1 gives an example of a zero-degree tilt 2D STEM micrograph and a 3D reconstruction from a +80 to -80 degree tilt series.

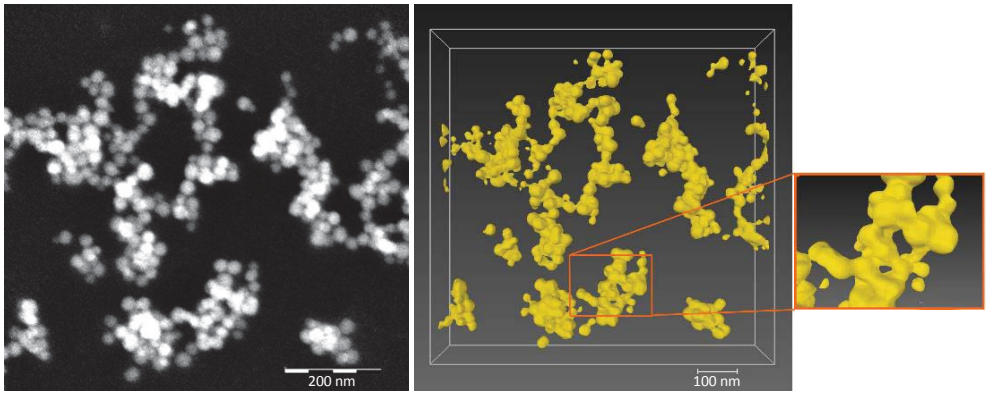

Figure 3.1: Silica nanoparticle gel sample (9 wt%, 70 nm thick sample) imaged with STEM. Left: zero-degree tit, 2D micrograph. Right: corresponding 3D reconstruction from a +80 to -80 degree tilt series. Image courtesy of C. Hamngren Blomqvist (Hamngren Blomqvist et al., 2016).

3.2 Polymer blended films

For Paper IV and V, free polymer blended films were prepared with ethyl cellulose (EC) and hydroxypropyl cellulose (HPC). The basis for each film is a homogeneous blend of 70% EC (w/w) and 30% HPC (w/w) dissolved in hydrous ethanol (95% v/v) at room temperature under stirring overnight. The resulting solution is sprayed onto a rotating Teflon drum by a moving spraying nozzle using a heated air flow in a modified fluidized-bed chamber originally designed for coating pellets. While drying, the ethanol evaporates which induces phase separation of the EC and HPC. As a consequence, EC-rich and HPC-rich phases form. This process is frozen by a high film viscosity which is reached at a certain ethanol concentration (Marucci et al., 2013). In contrast to EC, HPC is soluble in water or in the gastrointestinal tract and may act as a pore former when dissolved in water (Sakellariou and Rowe, 1995). Consequently, the connected HPC-rich phase can also be referred to as the pore phase. With a polymer content of 30% HPC, a connected, percolating pore phase is obtained with channels going from the drum-side of the film to the air-side (Marucci et al., 2009).

2D Images of the surface of film cross-sections were obtained by SEM. Prior to SEM imaging, small samples were embedded in epoxy-glue (resin and hardener) and cut in an ultramicrotome to expose the cross-section using first a glass knife, then a diamond knife. HPC was dissolved in water and the remaining EC was coated by a thin gold layer in order to increase the signal. 3D images were acquired by CLSM for which films were prepared with 6% fluorescent dye (0.005 m/m of glucose) labeled HPC. Figure 3.2 presents a 2D SEM and a 3D CLSM example.

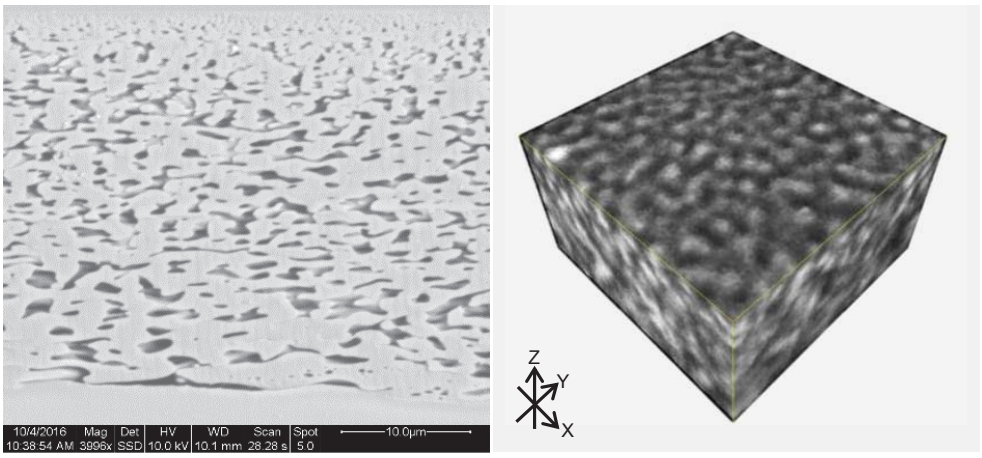

Figure 3.2: EC/HPC film sample (70/30 polymer content) imaged using SEM (2D) and CLSM (3D). Left: 2D cross-section after HPC leaching. EC-rich phase is shown in light gray and the pores, former HPC-rich phase, in dark gray. At the top (air side) and at the bottom (drum side) the epoxy-glue is also visible in light gray. Right: 3D image of a $23.57 \times 23.57 \times 17$ μm^3 section. Dark voxels correspond to the EC-rich phase and bright voxels to the HPC-rich phase. Dimension z goes from drum-side to air-side.

4 Image analysis

The image analyses conducted in this work can be divided into three main steps, noise reduction by filtering, image segmentation, and feature extraction. The first two steps are presented in Section 4.1. Section 4.2 presents further manipulations to the morphology of the foreground in a binary image. Features of interest here are particles and pore branching or end points. Particle detection is discussed in Section 4.3. In order to keep the notation easy, an image is regarded as a two-dimensional matrix $I = (I_{i,j})_{i=1,\dots,M;\ j=1,\dots,N}$, where each entry $I_{i,j}$ represents a pixel value on a gray-scale. The presented methods can be extended to three dimensions.

4.1 Image filtering and segmentation

An image may have to be enhanced prior to and even after segmentation. For example, filtering can be used to handle noise, to detect edges or to smoothen an image. Filtering involves a transformation of the image I using matrix operations often depending on a specified neighborhood around each pixel. In particular, an $n \times n$ neighborhood for $n \in \mathbb{N} = \{1, 2, \dots\}$ corresponds to an $n \times n$ matrix

$$w = (w_{k,\ell},\ \ell = -p, -p+1, \dots, p;\ k = -p, -p+1, \dots, p),$$

for $p = \lfloor \frac{n}{2} \rfloor$, where $\lfloor \cdot \rfloor$ denotes the floor function. A new, filtered image is obtained by

$$I_{i,j}^{new} = \sum_{k=-p}^{p} \sum_{l=-p}^{p} w_{k,\ell} I_{i+k,j+\ell}.$$

For a simple averaging filter, equal weights $w_{k,l} = \frac{1}{n \cdot n}$ are used. In this work, a more complex pixelwise adaptive Wiener filtering was used for Gaussian white noise reduction. This transformation is based on local estimates for the mean μ and the variance σ^2. The noise variance σ_n^2 is estimated by taking the average over all locally estimated variances. The transformed image I^{new} is obtained by setting

$$I_{i,j}^{new} = \hat{\mu}_{i,j} + \frac{\hat{\sigma}_{i,j}^2 - \hat{\sigma}_n^2}{\hat{\sigma}_{i,j}^2}(I_{i,j} - \hat{\mu}_{i,j}),$$

where $\hat{\mu}_{i,j}$ and $\hat{\sigma}_{i,j}^2$ refer to the locally estimated mean value and variance, respectively, and $\hat{\sigma}_n^2$ is the estimated noise variance. More details on filters can be found in Glasbey and Horgan (1995, Chapter 3).

Image segmentation, also referred to as binarization, is used to classify and discriminate regions of different pixel values in an image. Since the result is a binary image with black background and white foreground, image segmentation is also called binarization. Selecting an appropriate threshold for the binarization is crucial. A commonly used method applied to select the threshold is Otsu's method (Otsu, 1979), which is based on the histogram of the pixel values at L different levels, where the optimal threshold k^* corresponds to the value which minimizes the variance of pixel values below and above it. In particular, the histogram is divided into two classes with levels $[1, \ldots, k]$ in the first class and $[k+1, \ldots, L]$ in the second class for some threshold k. Let $\sigma_B^2(k)$ denote the between-class variance, then the optimal threshold k^* can be found by

$$\sigma_B^2(k^*) = \max_{1 \leq k < L} \sigma_B^2(k).$$

Figure 4.1 (B) presents an example of a binarization of a section of a EC/HPC film cross-section (A).

4.2 Morphological operations

The most common morphological operations are erosion and dilation with a structure element S moved along certain reference pixels collected in a set A. These operations can be used to remove small foreground objects, but are also very useful for more advanced distance and size analyses, for example. Let the group of pixels $S_{(i,j)}$ be the structure element S placed with its reference pixel at (i, j). Then the erosion of A by S can be defined as

$$A \ominus S = \{(i, j) : \ S_{(i,j)} \subset A\}$$

and the dilation of A by S is given by

$$A \oplus S = (A^c \ominus S)^c,$$

where A^c denotes the complement of A (Glasbey and Horgan, 1995, Chapter 5). Figure 4.1 (C) gives an example of an erosion by a pixelized disk with a diameter of 3 pixels.

Another useful morphological operation is sequential thinning and can be used for the shape characterization of objects. For example, A can be thinned until a skeleton is obtained. A skeleton is the union of minimally connected line segments with the thickness of one pixel. The algorithm by Couprie et al. (2007) thins the foreground while preserving its topology. In particular, homotopic thinning is applied, where so called simple points are deleted iteratively. Heuristically speaking, a simple point of a binary image is a pixel whose removal does not change the topology of the image. An ultimate homotopic skeleton is obtained if the resulting skeleton has no simple points. In order to ensure that the skeleton goes through regions of special interest, a constraint image can be added to the algorithm.

Figure 4.1 gives an example of a skeleton (D) obtained from a binary image (B). The skeleton has been dilated to increase its visibility. The skeleton of a pore structure can be used to identify pore branching and end points corresponding to branching and end points of the skeleton. Branching and end points can be classified by neighbor

counting, where an end point has one neighbor and a branching point at least three neighbors. For example, the skeleton of the large pore depicted in Figure 4.1 D has four end points and two branching points.

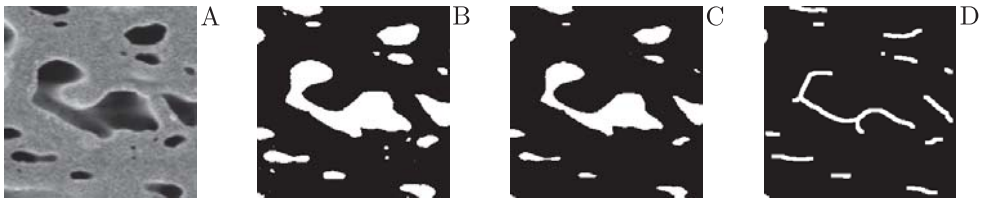

Figure 4.1: Example of an original gray-scale image (A) of size 250 by 250 pixels, (B) after segmentation and (C) after erosion by a pixelized disk with a diameter of 3 pixels. (D) shows the skeleton of the eroded image in (C) dilated by the same structure element.

4.3 Particle detection

For the detection of particles in two-dimensional micrographs, the circular Hough transform can be used (Atherton and Kerbyson, 1999). Let (x_0, y_0) denote the two-dimensional position of a circle center. Then a circle centered at (x_0, y_0) with radius $R > 0$ can be represented as the following system of equations

$$\begin{aligned} x &= x_0 + R\cos(\alpha), \\ y &= y_0 + R\sin(\alpha), \end{aligned}$$

where x and y trace the circle perimeter according to the angle $\alpha \in [-\pi, \pi]$. An alternative representation yields $R^2 = (x - x_0)^2 + (y - y_0)^2$. The Hough transform transforms the (x, y)-space to a three-dimensional parameter space (x_0, y_0, R). Candidates for points on the circle perimeter are pixels with a large gradient magnitude, which is calculated by the partial gradient images for column vectors $I(\cdot, j),\ j = 1, \ldots, N$ and row vectors $I(i, \cdot),\ i = 1, \ldots, M$

$$\begin{aligned} \frac{\partial I(\cdot, j)}{\partial x} &= 0.5\left(I(\cdot, j+1) - I(\cdot, j-1)\right), \\ \frac{\partial I(i, \cdot)}{\partial y} &= 0.5\left(I(i+1, \cdot) - I(i-1, \cdot)\right). \end{aligned}$$

The gradient magnitude is given by $\sqrt{\frac{\partial I}{\partial x}^2 + \frac{\partial I}{\partial y}^2}$ and the gradient direction by $\frac{180}{\pi} \arctan\left(-\frac{\partial I}{\partial y}, \frac{\partial I}{\partial x}\right)$. In order to detect circular objects, a circle with radius R is drawn around each candidate point and the points at the intersections are used as estimates for circle centers. This method can be extended to a range of radii $R_{min} \leq R \leq R_{max}$, see for instance Atherton and Kerbyson (1999).

5

Spatial point processes

This section presents basic definitions and characteristics of random spatial point processes which are fundamental to the spatial statistical analyses conducted in this work. The theory was mainly collected by Diggle (2014); Illian et al. (2008); Møller and Waagepetersen (2004) and Chiu et al. (2013). Henceforth, $\mathcal{B}(\mathbb{R}^d)$ denotes the Borel sets on $\mathbb{R}^d$ and $\mathcal{B}_0(\mathbb{R}^d)$ refers to the family of all bounded Borel sets on $\mathbb{R}^d$. The d-dimensional Lebesgue measure ν_d, also denoted by $|A|$, is used to measure the area of a set $A \subset \mathbb{R}^2$ for $d = 2$ or the volume of $A \subset \mathbb{R}^3$ for $d = 3$. $\partial(A)$ denotes the boundary of a set $A \subset R^d$, which corresponds to the circumference in $d = 2$ and the surface area in $d = 3$, respectively. $\mathbf{1}[\cdot]$ denotes the indicator function.

5.1 Basic definitions

Spatial point processes provide mathematical models for objects randomly or irregularly distributed on the plane ($d = 2$) or in space ($d \geq 3$). Point process models can be used to characterize the spatial arrangement of objects of interest and may contribute to solving problems in diverse fields, as for instance here, in materials sciences. In this work, point patterns or configurations $(x_1, \ldots, x_n)$ of silica particle centers and pore branching points observed in an observation window $W \subset \mathbb{R}^d,\ d = 2, 3$ are analysed as realizations of a point process X on $\mathbb{R}^d$. A sequence $X = \{X_i\}$ of random locations

$$X_i : \Omega \to \mathbb{R}^d,\ i = 1, 2, \ldots$$

on some probability space $(\Omega, \mathcal{A}, \mathbb{P})$ is a point process under two regularity conditions:

i) X is *locally finite* with a finite number of points $N_X(B) \geq 0$ in each bounded subset $B \in \mathcal{B}_0(\mathbb{R}^d)$,

ii) X is *simple*, in expression

$$\mathbb{P}(X_i \neq X_j) = 1 \quad \forall\ i, j \geq 1,\ i \neq j.$$

Let $\mathbf{N}$ denote the family of all locally finite counting measures and $\mathcal{N}$ be the smallest σ-algebra on $\mathbf{N}$ such that a point process X becomes a measurable mapping from a probability space $(\Omega, \mathcal{A}, \mathbb{P})$ into $(\mathbf{N}, \mathcal{N})$. Then there exists a distribution $P(A) = \mathbb{P}(X \in A)$, $A \in \mathcal{N}$ and the so called Palm distribution P_o at a typical point o of X

can be defined on $(\mathbf{N}, \mathcal{N})$. Heuristically speaking, P_o gives the conditional distribution $P(A|o)$ given that there exist a point of X in o.

The distribution of a point process can be used to define an *intensity measure* $\Lambda: \mathcal{B}(\mathbb{R}^d) \to [0, \infty)$ of a point process X such that

$$\begin{aligned}\Lambda(B) &= \mathbb{E}[N_X(B)] \\ &= \int_B \lambda(s)ds, \ B \in \mathcal{B}(\mathbb{R}^d),\end{aligned} \tag{5.1}$$

where (5.1) holds if Λ has a density $\lambda: \mathcal{B}(\mathbb{R}^d) \longrightarrow [0, \infty)$ with respect to the Lebesque measure, λ is called the *first-order intensity function*.

In order to study second-order characteristics of a point process X, the mean number of point pairs becomes of interest and is given by the *second-order moment measure*

$$\begin{aligned}\Lambda^{(2)}(B_1 \times B_2) &= \mathbb{E}[N_X(B_1)N_X(B_2)] \\ &= \alpha^{(2)}(B_1 \times B_2) + \Lambda(B_1 \cap B_2), \ B_1, B_2 \in \mathcal{B}(\mathbb{R}^d)\end{aligned}$$

determined by Λ and the *second-order factorial moment measure* $\alpha^{(2)}: \mathcal{B}(\mathbb{R}^d) \times \mathcal{B}(\mathbb{R}^d) \to [0, \infty)$ with

$$\alpha^{(2)}(B_1 \times B_2) = \mathbb{E}\left[\sum_{x \in X} \mathbf{1}[x \in B_1] N_X(B_2 \setminus \{x\})\right].$$

The variance of the number of points of X in B can be expressed by Λ and $\alpha^{(2)}$ and is given by

$$\begin{aligned}V(N_X(B)) &= \mathbb{E}(N_X(B)^2) - \Lambda(B)^2 \\ &= \alpha^{(2)}(B \times B) + \Lambda(B) - \Lambda(B)^2.\end{aligned}$$

Henceforth, the intensity measure is assumed to be locally finite. If not otherwise stated, the probability distribution of a point process, P_X, or the point process X itself is assumed to be invariant under translation and rotation. In other words, X is *stationary* and *isotropic* with

$$\mathbb{E}[N_X(B)] = \lambda \nu_d(B)$$

for some constant $\lambda > 0$ called the *intensity* of the point process X. For stationary point processes, a *reduced second-order moment measure* can be define as

$$\mathcal{K}(B) = \lambda^{-1} \mathbb{E}_o[N_X(B \setminus \{o\})]dx,$$

where $\mathbb{E}_o$ is the expectation with respect to the Palm distribution. The second factorial moment measure $\alpha^{(2)}$ can now be rewritten as

$$\alpha^{(2)}(B_1 \times B_2) = \lambda^2 \int_{B_1} \mathcal{K}(B_2 - x)dx,$$

where $B_2 - x$ denotes the set B_2 translated by the vector x.

Example 5.1 (Poisson process). X is called a *Poisson process* if it satisfies the following properties.

i) $N_X(B)$ is Poisson distributed with mean $\Lambda(B)$

ii) $N_X(B_1), N_X(B_2), \ldots$ are independent for pairwise disjoint sets $B_1, B_2 \in \mathcal{B}(\mathbb{R}^d)$.

If the Poisson process X is stationary, then $\Lambda(B) = \lambda\nu_d(B)$ holds and it is called the *homogeneous Poisson process*. The homogeneous Poisson process is often referred to as the completely spatially random (CSR) process as there are no interactions among points.

5.2 Functional summary characteristics

Summary characteristics describe the spatial distribution of points of a (finite) point process and are functions of distances between points. Non-parametric estimates of summary functions can be useful for validating fitted models and identifying interactions among points at certain inter-point distances. Two types of interaction may be distinguished, namely attraction and repulsion or inhibition, which both may occur in a single point pattern. Aggregated or clustered patterns with attraction among points tend to have more points within a short distance than CSR, and regular patterns arising from repulsion have less points within short distances than CSR. These effects are as schematically shown in Figure 5.1.

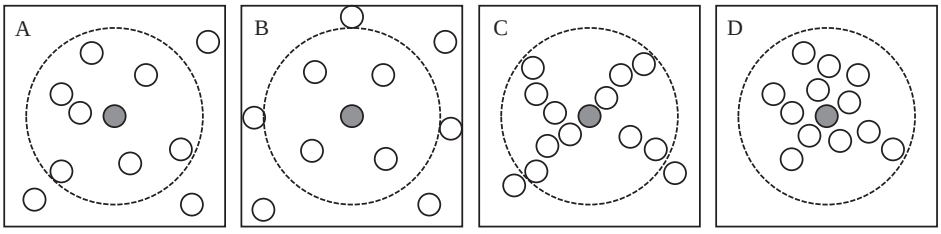

Figure 5.1: Schematic examples of different point patterns: A) CSR, B) regular pattern, C) and D) aggregated patterns with different inner cluster structures. In B there are less, whereas in C and D there are more points than in A within a certain distance indicated by the dashed circle around the origin marked in gray.

Usually a point process is observed in an observation window $W \subset \mathbb{R}^d$. Since the missing observations outside W may affect the estimation of summary functions, their estimators have to include some kind of edge correction. There are several methods available for dealing with edge effects involving guard areas, explicit weighting of observations close to the boundary of W, or wrapping W onto a torus. In the following only one example is given for each summary function.

5.2.1 Distance distribution functions

The *empty space function* $F:\ [0,\infty) \longrightarrow [0,1]$ gives the distribution of the distance from an arbitrary point $s \in \mathbb{R}^d$ to the nearest point in X. Considering the probability that a ball $b(s,r)$ centered at an arbitrary point $s \in \mathbb{R}^d$ with radius r does not contain any point of X, a cumulative distribution as a function of radius r can be obtained by

$$F(r) = 1 - \mathbb{P}(N(X \cap b(s,r)) = 0) \quad \forall r \geq 0.$$

A Kaplan-Meier estimator (Baddeley and Gill, 1997) can be constructed by

$$\widehat{F}(r) = 1 - \exp\left(-\int_0^r \left(\frac{\nu_{d-1}(\partial(X_{\oplus s}) \cap W_{\ominus s})}{\nu_d(W_{\ominus s} \setminus X_{\oplus s})}\right) ds\right) \quad \forall r \geq 0$$

for Minkowski operations $X_{\oplus r} = X \oplus b(o,r)$ and $W_{\ominus r} = W \ominus b(o,r)$ previously referred to as dilation and erosion in Section 4.

The distribution of the distance from a typical point o in X to its nearest neighbor in X is also an often used summary function. Given that there is a point of X in o, the distance to the nearest point is smaller than r if and only if there is at least one other point of X in the ball $b(o,r)$. Hence, the nearest neighbor distance distribution function $G:\ [0,\infty) \longrightarrow [0,1]$ can be defined as

$$G(r) = P_o(N_X(b(o,r) \setminus \{o\}) > 0) \quad \forall r \geq 0.$$

The G-function can be estimated by

$$\widehat{G}(r) = \frac{1}{n_{\ominus r}} \sum_{x \in W_{\ominus r}} \mathbf{1}[N_X(b(x,r) \setminus \{x\}) > 0] \quad \forall r \geq 0$$

following a minus-sampling scheme based on an eroded observation window $W_{\ominus r}$ containing $n_{\ominus r}$ points.

The empty space function and the nearest neighbor distance distribution function can be combined to the so called J-function

$$J(r) = \frac{1 - G(r)}{1 - F(r)} \quad \forall r \geq 0,$$

for $F(r) < 1$. A plug-in estimator for the J-function can be constructed with estimators for G and F.

Example 5.2. (F, G and J for Poisson, regular and cluster process).

- *Poisson process*: $F(r) = G(r)$ and, hence, $J(r) = 1$ for $r \geq 0$.
- *Regular process*: Inter-point distances tend to be larger compared to CSR and distances from an arbitrary location in W to the nearest point smaller. Consequently, $F(r) \geq G(r)$ and $J(r) > 1$.
- *Cluster process*: Inter-point distances tend to be smaller compared to CSR and distances from an arbitrary location in W to the nearest point larger. Consequently, $F(r) \leq G(r)$ and $J(r) < 1$.

5.2.2 Second-order characteristics

A common second-order characteristic is *Ripley's K-function* $K : [0, \infty) \to [0, \infty)$ also known as the second reduced moment function since it is defined as

$$\begin{aligned} K(r) &= \mathcal{K}(b(o, r)), \\ &= \lambda^{-1}\mathbb{E}_o(N_X(b(o, r) \setminus \{o\})) \quad \forall r \geq 0. \end{aligned}$$

In other words, $\lambda K(r)$ gives the expected number of points of X within a ball $b(o, r)$ without counting o itself given that there is a point of X in o. Using Ripley's isotropic edge correction, the following estimator for the K-function is obtained by

$$\widehat{K}(r) = \frac{|W|}{n(n-1)} \sum_{i=1}^{n} \sum_{j \neq i} w_{ij}^{-1} \mathbf{1}(d_{ij} < r) \quad \forall r \geq 0$$

for pairwise inter-point distances $d_{ij} = \|x_i - x_j\|$ and $n = N_X(W)$ observed points of X in W. The weights are given by

$$w_{ij} = \frac{\nu_{d-1}(\partial(b(x_i, d_{ij}) \cap W))}{\nu_{d-1}(\partial b(x_i, d_{ij}))},$$

which is the proportion of the circumference ($d = 2$) or surface area ($d = 3$) of the ball $b(x_i, d_{ij})$ lying inside W. The weights are defined such that $w_{ij} = 1$ if $b(x_i, d_{ij}) \subset W$.

A variance stabilizing transformation of the K-function, is given by the L-function $L : [0, \infty) \to [0, \infty)$ defined as

$$L(r) = \sqrt[d]{\frac{K(r)}{\nu_d(b(o, 1))}} \quad \forall r \geq 0.$$

In Paper V, we generalize the K-function for inhomogeneous and anisotropic point processes.

The *pair-correlation function* $g : [0, \infty) \longrightarrow [0, \infty]$ is a normalized transform of the derivative of the K-function given by

$$g(r) = \frac{\frac{dK(r)}{dr}}{\nu_{d-1}(\partial b(o, r))} \quad \forall r > 0.$$

The g-function is typically estimated by kernel smoothing with an Epanechnikov kernel.

Example 5.3. (K, L and g for Poisson, regular and cluster process for $d = 2$).

- *Poisson process*: $K(r) = \pi r^2$, $L(r) = r$ and $g(r) = 1$ for $r \geq 0$.
- *Regular process*: Within short distances, there tend to be less points than in the CSR such that $K(r) \leq \pi r^2$, $L(r) \leq r$ and $g(r) \leq 1$.
- *Cluster process*: Within short distances, there tend to be more points than in the CSR such that $K(r) \geq \pi r^2$, $L(r) \geq r$ and $g(r) \geq 1$.

5.2.3 Third-order characteristic

In order to describe the inter-point behavior of a point process on a higher-order, the behavior between more than two points can be taken into account. Third-order characteristics have been introduced in Schladitz and Baddeley (2000) and Rajala (2010), for example. The mean number of r-close triplets summarized in the triplet function $T : [0, \infty) \longrightarrow [0, \infty)$ with

$$T(r) = \frac{1}{2\lambda^2}\mathbb{E}_o \sum_{i,j:x_i,x_j \in X \cap b(o,r)\setminus\{o\}} \mathbf{1}[0 < d_{ij} < r] \quad \forall r \geq 0.$$

The T-function can be estimated by a minus-sampling scheme, where

$$\widehat{T}(r) = \frac{|W|^2}{n(n-1)} \frac{|W_{\ominus r}|}{2n_{\ominus r}} \sum_{i:x_i \in X \cap W_{\ominus r}} \sum_{j \neq i} \sum_{k \neq i,j} \mathbf{1}[d_{ij} < r]\mathbf{1}[d_{ik} < r]\mathbf{1}[d_{jk} < r].$$

The clustering function $c : [0, \infty) \longrightarrow [0, 1]$ sets the number of triplets in $b(o, r)$ in relationship to the theoretical number of possible triplets $n_{o,r} = \frac{1}{2}(\delta(o)^2 - \delta(o))$ with $\delta(o) = \sum_{j=1}^{n} \mathbf{1}[0 < \|o - x_j\| \leq r]$ such that

$$c(r) = \begin{cases} \frac{1}{n_{o,r}}\mathbb{E}_o \sum_{i,j:x_i,x_j \in X \cap b(o,r)\setminus\{o\}} \mathbf{1}[0 < d_{ij} < r] & , \ \delta(x_i) > 2 \\ 0 & , \ \text{else} \end{cases}$$

for all $r \geq 0$. c can be estimated in a similar way as T by a minus-sampling scheme.

5.2.4 Mean cluster size function

On joining several points of a planar point process in a cluster, another higher-order characteristic can be defined for the mean cluster size based on the diameter of a cluster, the so called diameter of gyration (Khan et al., 2014). Let us assume there are $k = 1, \ldots, K$ clusters of points. For polymer chains, the diameter of gyration D_k of the kth chain measures the distance of joints of the chain to the center of mass. In a point process setting the squared radius of gyration for the kth cluster with n_k points can be calculated by

$$\left(\frac{D_k}{2}\right)^2 = \frac{1}{n_k} \sum_{i=1}^{n_k} \|x_i - \bar{x}\|^2 = \frac{1}{2n_k^2} \sum_{i=1}^{n_k} \sum_{j=1}^{n_k} d_{ij}^2$$

with center of mass

$$\bar{x} = \frac{1}{n_k} \sum_{i=1}^{n_k} x_i.$$

The mean cluster size function $M : [0, \infty) \longrightarrow [0, \infty)$ is defined as

$$M(r) = \frac{1}{K} \sum_{k=1}^{K} (D_k(r)) \quad \forall r \geq 0$$

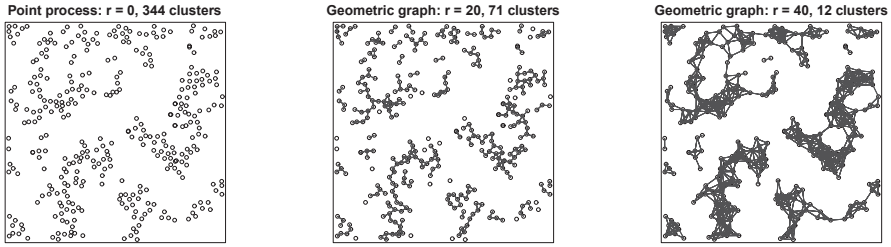

Figure 5.2: Definition of clusters using a geometric graph with edge length $r = 0$ (left), $r = 20$ (middle) and $r = 40$ (right) in a 600×600 observation window.

where $D_k(r)$ is the size of the kth cluster constructed by a geometric graph (Penrose, 2003) placing an edge between two points if the distance between them is smaller than r. As a result, each cluster is formed by a set of points connected in the graph as depicted in Figure 5.2.

In order to account for edge effects, a weighted average of the diameter of gyration was used for the estimation of the M-function such that

$$\widehat{M}(r) = \sum_{k=1}^{K} w_k D_k(r) \quad \forall r \geq 0,$$

where the weight $w_k = \frac{n_k}{n}$ is the proportion of the number of points in the kth cluster. This weighting method emphasizes large cluster, where many point pairs can be observed. Alternatively, a minus-sampling scheme can be used.

Example 5.4. (T and M for Poisson, regular and cluster process for $d = 2$).

- *Poisson process*: $T(r) = \frac{1}{2}\pi(\pi - \frac{3}{4}\sqrt{3})r^4$ for $r \geq 0$.
- *Regular process*: The mean number of r-close triplets tends to be smaller, whereas the mean interpoint distance in a cluster with maximal edge length r tends to be larger compared to CSR at short distances.
- *Cluster process*: The mean number of r-close triplets tends to be larger. The mean interpoint distance in a cluster with maximal edge length r tends to be smaller compared to CSR for tight clusters. If the clusters contain many particles or are more branched with connected points spreading over larger distances, the mean size of a cluster can be larger compared to CSR.

For the examples in Figure 5.1, we have $T_{\mathrm{B}} < T_{\mathrm{A}} < T_{\mathrm{C}} < T_{\mathrm{D}}$. In contrast, the expected size of a cluster for a certain edge length r tends to be smaller for clustered processes than for regular resulting in $M_{\mathrm{B}} > M_{\mathrm{A}} > M_{\mathrm{C}} > M_{\mathrm{D}}$. Due to its physical derivation, M might be easier to interpret than T and may reveal further structural characteristics.

5.3 Finite pairwise interaction Gibbs processes

The Poisson process often serves as a reference model and underlies many other models. For example, the popular and wide class of Cox processes is a generalization of inhomogeneous Poisson processes with a random intensity function $\lambda(x)$. Cox processes can be used to model aggregated or clustered patterns, where clusters of points arise by some external heterogeneity or environmental variability. However, the points of a Cox process are still conditionally independent given the intensity function. Here, another flexible class of point processes models is introduced, namely the spatial exponential family of Gibbs processes, sometimes also called Markov point processes. Gibbs processes allow for interactions with local or Markovian dependence between points. As mentioned in Section 1.1, Gibbs processes have their origin in statistical mechanics and physics. In statistics, it is often practical to condition on the number of points n in the observation window W. In this case a Gibbs process is defined by its density

$$f_n(x_1, \ldots, x_n) = \frac{\exp(-E(x_1, \ldots, x_n))}{Z_n}$$

with respect to a Poisson process with intensity $\lambda = 1$. The function $E : \mathbb{R}^{n \times d} \longrightarrow (-\infty, \infty]$ assigns an energy to a point configuration $\boldsymbol{x} = (x_1, \ldots, x_n)$ and $Z_n = \mathbb{E}[\exp(-E)]$ is a normalizing constant. The density f_n is well defined if Z_n is integrable. Then, $Z_n < \infty$, which holds by considering finite configurations with $n < \infty$ points.

For an isotropic finite pairwise interaction process, the energy function can be written in the form of

$$E(x_1, \ldots, x_n) = \sum_i \alpha(x_i) + \sum_{i<j} \phi(d_{ij}),$$

for pairwise distances $d_{ij} = \|x_i - x_j\|$. The function $\alpha : \mathbb{R}^d \longrightarrow \mathbb{R}$ is called the chemical activity function and describes the likelihood of a point being located at $x \in W$. For a stationary process, $\alpha(x) = \alpha,\ \alpha \in \mathbb{R}$ is a constant. The function describing pairwise interactions $\phi : (0, \infty) \longrightarrow \mathbb{R} \cup \{\infty\}$ is called the pair-potential function and $\exp(-\phi(\cdot))$ the interaction function.

In Paper V, anisotropic pair-potential functions depending not only on the length of pairwise difference vectors $x_i - x_j$, but also on their orientation, are introduced. The pair-potential function can be extended further to higher-order interactions and more complicated neighborhoods.

The Papangelou conditional intensity at a location $u \in W$ is defined as

$$\lambda(u; \boldsymbol{x}) = \frac{f_n(\boldsymbol{x} \cup \{u\})}{f_n(\boldsymbol{x} \setminus \{u\})}$$

for $f_n(\boldsymbol{x} \setminus \{u\}) > 0$ and $\lambda(u; \boldsymbol{x}) = 0$ otherwise.

Example 5.5. (Common pairwise Gibbs processes).

- *Poisson process*: The Poisson process is a member of the family of Gibbs processes with density
$$f_n(x_1, \ldots, x_n) = \frac{\exp(-n\alpha)}{Z_n}$$
with pair-potential function $\phi(r) = 0$ for all $r > 0$.

- *Regular process*: For regular processes $\phi(r) \leq 0$ for $r > 0$ and the process is locally stable if $\int_W \exp(-\phi(s))ds < \infty$. A popular model for regular patterns is the Strauss process with
$$\phi_S(r) = \beta \mathbf{1}[r < R],\ R > 0$$
where each R-close point pair contributes with interaction strength $\gamma = \exp(-\beta)$, $\beta \in \mathbb{R}$, $0 < \gamma < \infty$. $\beta = 0$ and $\gamma = 1$, respectively, correspond to a Poisson process and $\beta > 0$ or $\gamma < 1$ yield repulsion.

- *Cluster process*: For clustered processes $\phi(r) \geq 0$, f_n is generally not well defined (Møller and Waagepetersen, 2004, p.84). The Strauss process with $\beta < 0$ or $\gamma > 1$ can be used to model attraction among points. For large γ, however, points tend to form one large cluster.

- *Lennard-Jones process*: A pair-potential function allowing for both repulsion and attraction on an infinite range is the Lennard-Jones potential, where
$$\phi_{LJ}(r) = 4\epsilon \left(\left(\frac{\sigma}{r}\right)^{m_1} - \left(\frac{\sigma}{r}\right)^{m_2} \right),$$
for $m_1 > m_2$, $r > 0$. The so called 12-6 Lennard-Jones potential is of special interest in this work as it is motivated by repulsive electrostatic ($m_1 = 12$) and attractive van der Waals ($m_2 = 6$) forces. The pairwise interaction changes from repulsion to attraction at the characteristic distance $\sigma > 0$ where the potential becomes zero. The parameter $\epsilon \geq 0$ determines the interaction strength.

Figure 5.3 presents the pair-potential and interaction functions for the Poisson, repulsive Strauss and 12-6 Lennard-Jones potential.

Gibbs processes are mathematically challenging, especially for strong attraction between points. There are several methods available for the parameter estimation of finite Gibbs processes with pairwise interactions. Several maximum likelihood methods have been suggested with different ways to approximate the often intractable normalizing constant. The first maximum likelihood method with an approximation of the normalizing constant was introduced by Ogata and Tanemura (1981) for sparse data. Also for sparse data, Penttinen (1984) used a stochastic version of the Newton-Raphson algorithm to approximate the maximum likelihood. The Monte Carlo scheme in Penttinen (1984) requires a new sample in each iteration and convergence may not be reached. This was improved by using importance sampling in the Monte Carlo approximation in Geyer and Thompson (1992). Besag (1975) presented a maximum pseudo-likelihood

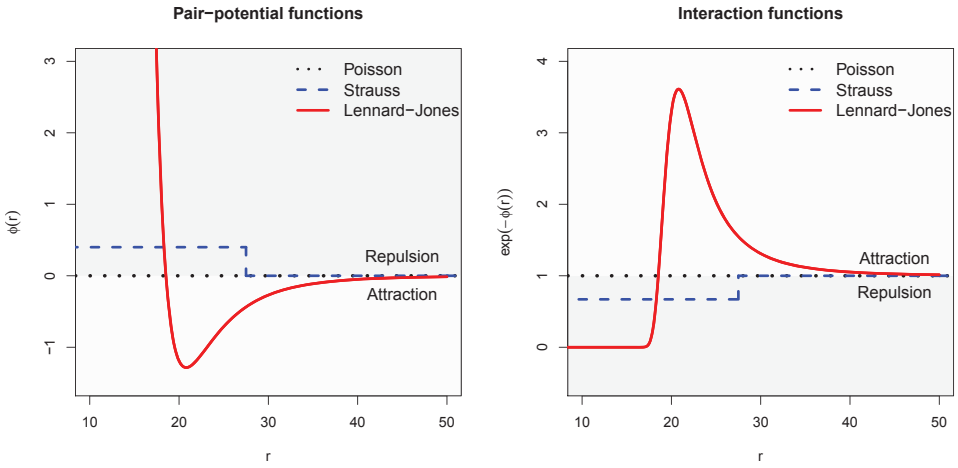

Figure 5.3: Examples of pair-potential functions ϕ and interaction function $\exp(-\phi)$ for the Poisson process with no interaction, the repulsive Strauss process and the 12-6 Lennard-Jones process with attraction between points after some hard-core distance.

method based on the Papangelou conditional intensity, where the normalizing constant cancels out. Takacs-Fiksel estimation was later developed in Takacs (1986) as a more general parameter estimation approach inspired by the method of moments. The maximum pseudo-likelihood method can be seen as a special case of Takacs-Fiksel estimation (Diggle et al., 1994). Recently, a Bayesian smoothing technique for a semi-parametric estimation of the likelihood function was added by Heikkinen and Penttinen (1999). Comparisons of different methods and further references can be found in Baddeley and Turner (2000); Diggle et al. (1994); Mateu and Montes (2001); Møller and Waagepetersen (2004).

Markov chain Monte Carlo with Metropolis-Hastings algorithms are popular for the simulation of Gibbs processes with an unnormalized density on a bounded region (Møller and Waagepetersen, 2004, p.107). Alternative simulation methods are birth-and-death procedures, simulated tempering and exact or perfect simulation (Kendall and Møller, 2000; Møller, 1999; Møller and Waagepetersen, 2004).

In this study, we typically use the logistic regression version of the maximum pseudo-likelihood estimation as discussed in Baddeley et al. (2014) for parameter estimation. It is computationally simple because it can be computed with standard software. For the estimation of the step-function potential, a Bayesian smoothing technique as suggested in Heikkinen and Penttinen (1999) was used since it can handle large variations of parameter estimates due to low point counts in the design matrix. For each estimation, minus-sampling was chosen as edge correction (Illian et al., 2008, p.185 f.). A Metropolis-Hastings algorithm for the conditional case of point processes with a density as presented in (Møller and Waagepetersen, 2004, p.109) was followed for pattern

simulation. A guard area as discussed in Mateu and Montes (2001) with a fixed density was used to correct for missing data outside the observation window. The guard window size was chosen to have an additional side length of four times the interaction range. As the interaction range is theoretically infinite for the Lennard-Jones potential, the interpoint distances were truncated to obtain a finite range.

6

Summary of appended papers

The papers appended to this thesis can be divided into two groups according to the respective material studied. The first group consists of three papers dealing with colloidal silica particle aggregation. The second group contains two papers on EC/HPC polymer blended films. The five appended papers are introduced in the context of this thesis. Since the emphasis in all papers is on the developed methods, the main components of each method are presented. Furthermore, the most important results of each work are highlighted.

6.1 Paper I-III: Colloidal nanoparticle gels

Paper I: Estimation of mass thickness response of embedded aggregated silica nanoparticles from high angle annular dark-field scanning transmission electron micrographs

In Paper I, we studied 2D micrographs of nanosized silica particle gels obtained by STEM. The intensity of each pixel of the obtained 2D projections contains information about the silica mass thickness along the projection axis. The goal was to find a method for estimating the actual silica mass thickness response and, hence, the number of particles at each pixel in order to draw conclusions on the original 3D structure. In particular, the intensity $I(x, y)$ at position (x, y) is modeled as a power function g of the mass thickness $\alpha(x, y)$ with additive zero-mean Gaussian noise $e_{x,y}$, in expression

$$I(x, y) = b + cg(\alpha(x, y)) + e_{x,y}, \tag{6.1}$$

where b and c are constants. The parameters involved were estimated by maximizing the log-likelihood while iterating the positions of artificial particles and varying the remaining parameters using a grid search. A major achievement was a computationally efficient program that accurately approximates the maximum of the log-likelihood function in feasible time. A key component here was to control the lowering of the parameter driving the cooling regime in a simulated annealing algorithm used for iterating the particle positions.

In a validation study, silica particles were simulated by a Poisson point process model and micrographs were generated using a power function with chosen fixed parameters. The results indicated that the shape parameters of the power function were estimated correctly and the iterated particle positions showed a good fit. Finally, the

method was evaluated on experimental micrographs and we showed that a power function performs statistically significantly better than a linear function. By fitting the parameters for the intensity power function, a non-unique solution to the 3D particle positions and therewith an estimate for the silica mass thickness was obtained. This result is an important step towards a full 3D particle position reconstruction from 2D images. Figure 6.1 gives an example on a section of a micrograph and one possible solution of the 3D particle configuration.

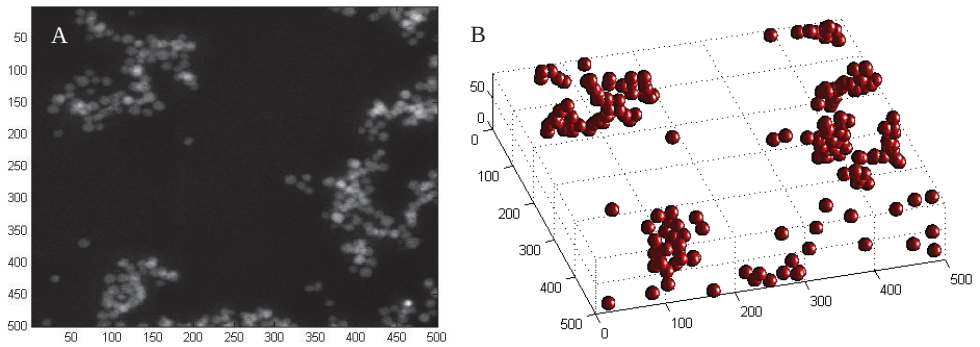

Figure 6.1: Example of STEM micrograph in a 500 × 500 nm section (A) and one of several possible 3D reconstructions of silica particle positions (B).

Paper II: From static micrographs to particle aggregation dynamics in three dimensions

In Paper I, we developed a method for estimating the mass thickness of nanosized silica particle gel samples from 2D STEM micrographs. As a result, we obtained estimates of mass thickness of the silica at each pixel, but not their exact location along the projection axis in the direction of the electron beam. For a complete 3D reconstruction of the particle positions, it is important to understand the spatial arrangement of the particles and their degree of connectivity. The silica particles form a connected network spanning through the sample, where clusters of particles can be of different typical shapes. The final static particle configuration and connectivity depends on the dynamic particle aggregation process.

In this study, the diffusion limited cluster aggregation (DLCA) and reaction limited cluster aggregation (RLCA) processes were evaluated. The major challenge was to be able to draw conclusions on a 3D dynamic process from static 2D images. Our developed method is based on a quantitative comparison of experimental micrographs to artificial micrographs created from DLCA and RLCA simulations. The chosen probabilities of aggregation were $p = 1$ for the DLCA and $p = 0.1,\ 0.01,\ 0.001,\ 0.0001$ for the RLCA simulations. The simulated particle configurations and the relationship (6.1) were used to generate the artificial micrographs. Subsequently, particles are

detected by a newly composed particle detection algorithm based on standard tools from image analysis. Finally, the resulting point patterns of experimental and artificial particle centers were compared by common summary functions from spatial statistics, the empty space function and the L-function, and more specific summary functions for cluster analysis, the clustering function and the mean cluster size function. The latter was developed in this work. The results for all four summary functions are shown in Figure 6.2.

In a least square approach collecting all information from the different summary functions, we drew a combined inference on the probability of aggregation that can be associated with the gel samples. We showed that each aggregation scenario captures different structure characteristics of the gel samples, however, overall a very small probability of aggregation (< 0.0001) seems most suitable for modeling the silica particle aggregation.

Paper III: Colloidal particle aggregation in three dimensions

In Paper III, we extended the 2D study on the DLCA and RLCA models for particle aggregation in Paper II to three dimensions. For this purpose, a new 3D particle detection algorithm was developed and the mean cluster size function was implemented for 3D point patterns. In a first approach of estimating the probability of aggregation for the given data, again experimentally obtained and simulated structures were compared by means of spatial summary functions as presented in Figure 6.3. In a second approach, we used a relationship between the probability of aggregation p and the pair-potential function ϕ that describes the interactions between the particles by

$$p = 2a \int_0^\infty \frac{1}{r^2} \exp\left(\frac{-\phi(r+2a)}{k_T}\right) dr,$$

for two approaching particles of radius a and distance $r > 0$ between their center points, where k_T is a scaling constant. For a true physico-chemical potential, $k_T = k_B T$, where k_B is the Bolzmann constant and $k_B T$ gives the thermal energy of the system at room temperature. In order to estimate the pair-potential function in a statistical model, three different finite pairwise interaction Gibbs point process models were fitted to the data. The model choice was motivated by commonly used potentials in colloidal science, namely the Lennard-Jones and the square-well potential. We also fitted a step pair-potential function with several jumps in an estimation procedure with weaker modeling assumptions.

In Paper II artificial micrographs were simulated from generated point patterns and particles were detected in both experimental and simulated micrographs. This was done in order to get comparable point patterns as the 2D detection of projected particles has a relatively high error rate. In contrast, the 3D data holds more information about the number of particles present in the imaged sample due to no loss of information caused by projection of particles onto a 2D image. This facilitates the detection of particles. Additionally, noise and artefacts such as the missing wedge effect common in electron tomography make the reconstruction of a 3D micrograph more challenging than in two dimensions. That is why, no artificial 3D micrographs were created.

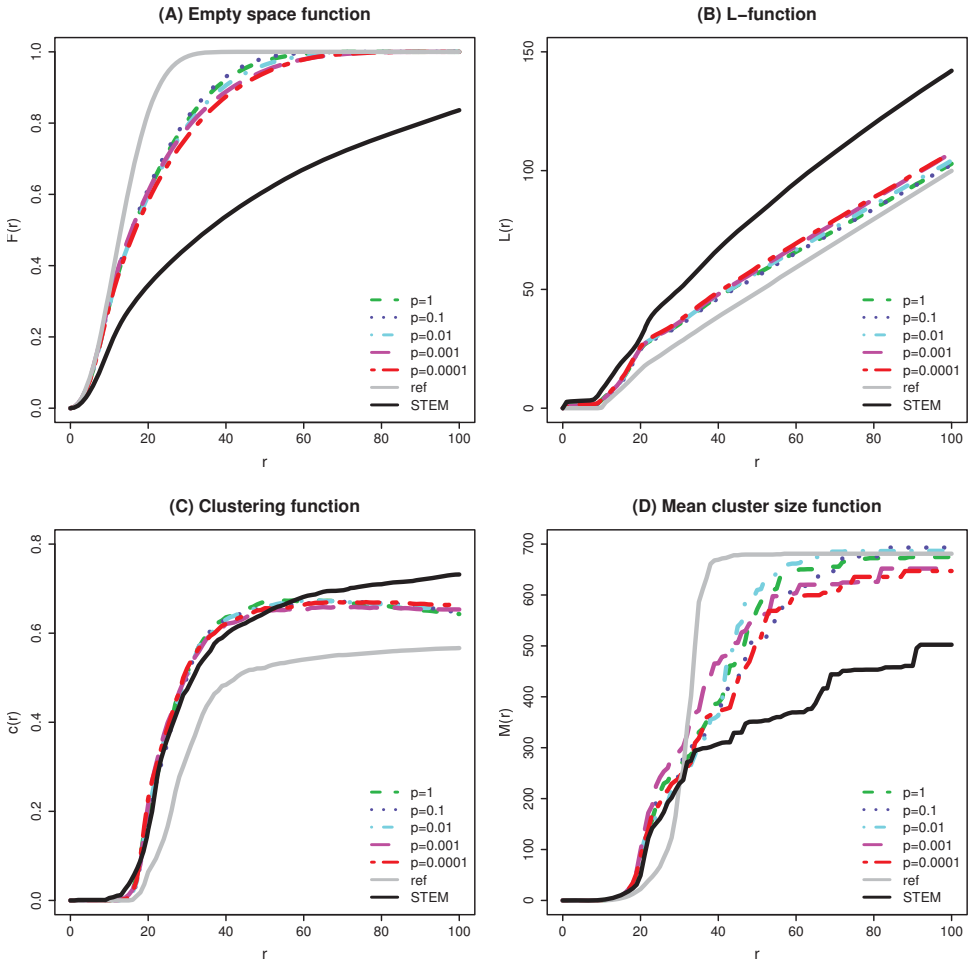

Figure 6.2: In 2D: (A) Empty space function F, (B) L-function, (C) clustering function c, and (D) mean cluster size function M pooled for point patterns from cluster aggregation simulations with five different probabilities of aggregation p, realizations of a reference point process (ref) without particle aggregation, and 2D STEM micrographs.

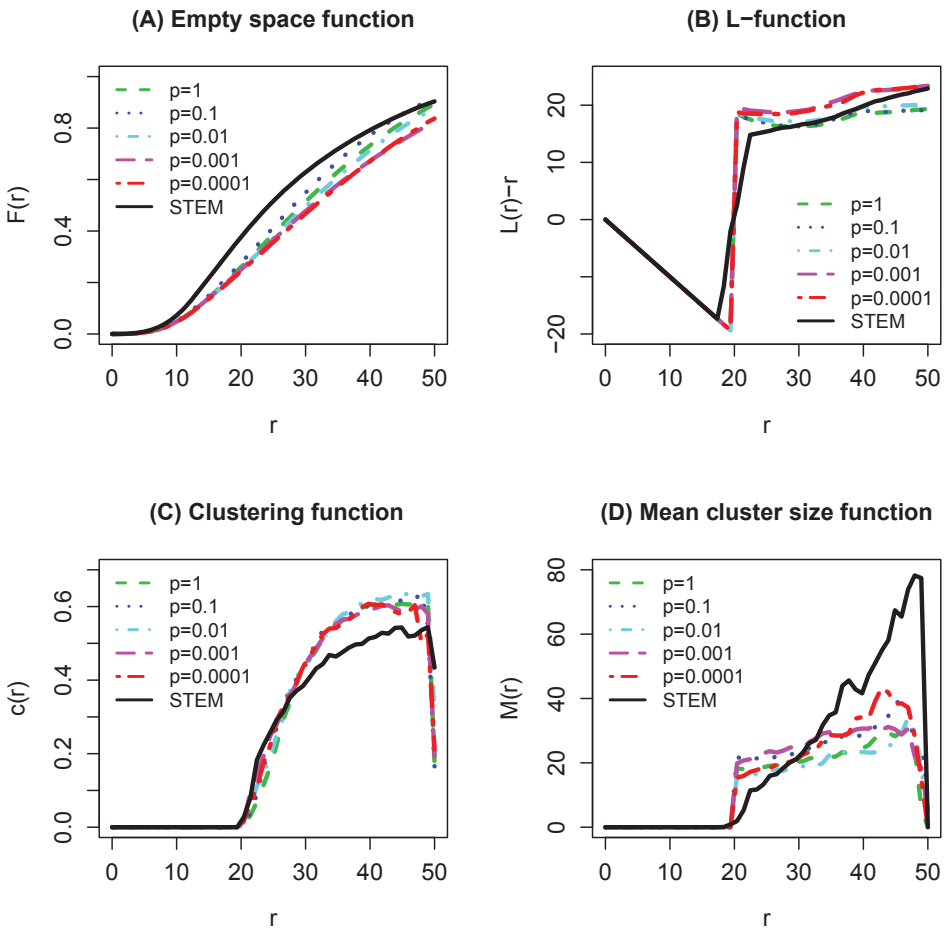

Figure 6.3: In 3D: (A) Empty space function F, (B) L-function, (C) clustering function c, and (D) mean cluster size function M pooled for point patterns from cluster aggregation simulations with five different probabilities of aggregation p and 3D STEM micrographs.

Interestingly, all simulation summary functions are close to each other in both the 2D and the 3D study. However, the curves corresponding to the STEM data lie much closer to those of the simulations in 3D than in 2D. We concluded that important information about the aggregation regime can be obtained from 2D micrographs, but that a 3D data analysis is needed to detect structural details and to estimate the probability of aggregation. We found that neither DLCA nor RLCA separately are fully satisfactory models for the silica particle aggregation, but that a combination of them could be more feasible. Furthermore, we showed that static models such as the Gibbs model can be linked to a dynamic process.

6.2 Paper IV and V: Polymer blended films

Paper IV: Characterization of pore structure of polymer blended films used for controlled drug release

The controlled release of an oral formulation is often achieved by coating the formulation with a polymer film, where the structure of the film governs the release mechanism. For insuring high quality treatments, mass transport through porous pharmaceutical coatings needs to be understood and controlled. Spatial characterization and modeling of the porous media may provide valuable knowledge supplementary to experiments.

In this work, an EC/HPC polymer blended film was studied, where only HPC is water-soluble and acts as a pore former. On the attempt of understanding and controlling the release mechanism of the film, a characterization of the pore space was developed based on 2D images. In particular, the motivation for this study was a difference in permeability found between two films with different polymer viscosities. As nearly the same amount of leached HPC was measured, the question arose in which way the pore structures of the two films differed.

In this study, series of overlapping 2D SEM images of film cross-sections were available from three different parts of the film. After merging images from the same part and having achieved a reasonable segmentation of the two polymer phases, we conducted an image analysis on the size and shape of the pores. Figure 6.4 presents the experimental and statistical analysis set up on the example of average pore size in film layers going from drum-to-air-side.

Results on the pore size had already been obtained in related studies. That is why we focused on investigating and comparing different pore shape measures. An analysis of variance of all considered pore characteristics indicated a statistically significant difference between the two films in the number of branching and end points of the pore skeleton. Consequently, we found that the more permeable film seems to have a better pore connectivity due to more elongated shapes. This conclusion was in line with hypotheses developed during experiments, which had not been deduced from a statistical analysis before.

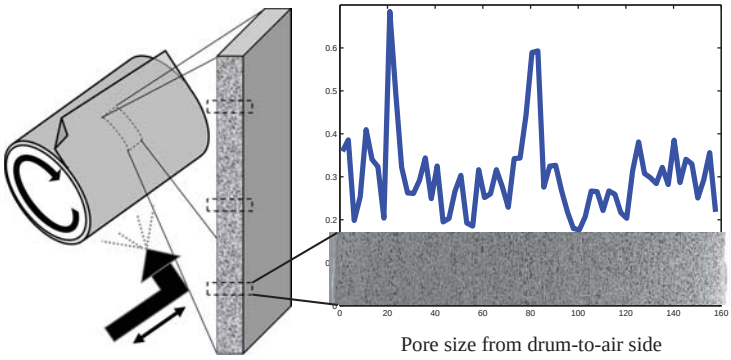

Figure 6.4: Experimental set up of free polymer blended films sprayed onto a rotating Teflon drum. Cross-sectional images were taken from three parts of each sample and pore characteristics were analyzed as a function of film depth from drum-to-air-side. Here, the average pore size measured in number of pixels is shown, where a pixel is of size 37 nm.

Paper V: A three-dimensional anisotropic point process characterization for pharmaceutical coatings

In Paper IV, we drew the conclusion that the permeability of EC/HPC polymer blended film depends on the pore connectivity, which, in turn, can be related to the number of pore branching and end points. In Paper V, we developed a methodology to validate this result in 3D. For this purpose, new free films were prepared and imaged by 3D CLSM. We again extracted characteristics of the pore structure, which required a more advanced image analysis than in 2D.

Prior to the statistical analysis, a 3D ultimate homotopic skeleton of the pore structure was obtained. The skeleton was used to identify isolated pores, pore channel end points and branching points of at least three pore channels. Especially, the number, location and connection of pore branching points was of interest for later analyses. In order to save information on which branching points are connected in the pore structure, the skeleton was translated into a spatial graph. Then, the graph was reduced to the branching points by deleting all other nodes from the graph that were not branching points.

We used and developed point process theory to characterize the branching structure. Point patterns, extracted by identifying branching points of the skeleton through the pore channels, were both inhomogeneous and anisotropic. Therefore, we introduced a directional version of the inhomogeneous K-function to study the anisotropy and then suggested two alternative ways to model the anisotropic 3D branching point structure. First, we applied a linear transformation to the data to obtain close to isotropic patterns and subsequently fitted isotropic inhomogeneous finite pairwise interaction Gibbs models to the transformed pattern. Second, we included the anisotropy directly in two Gibbs models with anisotropic pair-potential functions. The model choice was once more inspired by molecular dynamics. We compared models with a Lennard-

Jones pair-potential function to the Strauss model and its generalization with a step pair-potential function. Whereas the Strauss model only allows for either attraction, inhibition or no interaction between points, the type of interaction can vary for different ranges in the step-function model.

We found that the models based on linear transformations were not applicable. The model with an anisotropic Lennard-Jones pair-potential function was promising, but did not capture mid-range inhibition present in the data. Being more flexible, the Gibbs model with an anisotropic step pair-potential function performed the best. Figure 6.5 presents the anisotropic pair-potential functions and the corresponding goodness-of-fit analysis based on the inhomogeneous and anisotropic K-function.

Three important conclusions on the film pore structure were drawn. First, it was found that the number of branching points decreases linearly from upper to lower film layers. Second, the pore branching points appear to be connected to their nearest neighbor by almost vertical pore channels. Third, the vertical pairwise interaction among branching points seems to be different from horizontal interaction. The results are not only important for identifying important features of the pore structure, more importantly, we also showed the usefulness of anisotropic pair-potential functions in general.

The 3D inhomogeneous and anisotropic model for the branching points in a porous polymer blended film can be used as input for a full model of the pore structure. In a simple first marked point process model, spheres can be constructed around each branching point with the local pore radius as the size parameter. Consequently, the spheres can be connected by necks using information on the branching point connectivity and pore throat thickness obtained by the conducted image analysis. Alternatively, the points can be connected by straight lines around which a Euclidean distance field perturbed by a random field forms the pore throat.

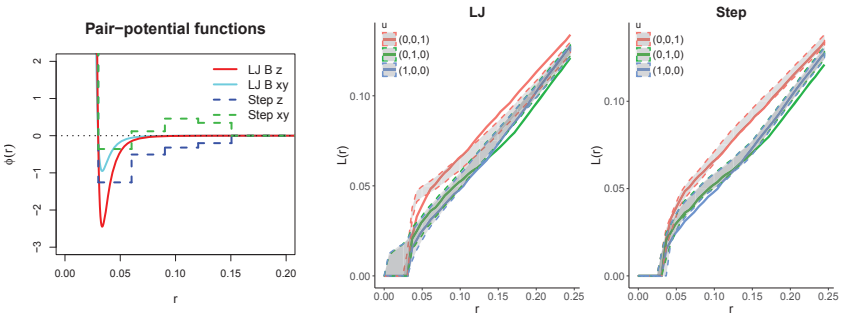

Figure 6.5: Left: anisotropic pair-potential functions for the Lennard-Jones (LJ) and the step-function (Step) model with different parameters horizontally (zy) and vertically (z). Middle and right: goodness-of-fit plots for Model LJ and Step based on the L-function in three directions $x = (1, 0, 0)$, $y = (0, 1, 0)$ and $z = (0, 0, 1)$ within a double cone with opening angle of $\pi/3$. The dashed lines give the global envelope bounds based on 2499 simulations. The thick solid curves correspond to the data.

7 Conclusions

In this work two different porous materials have been analyzed with established and newly developed methods from image analysis and spatial statistics. The introduction and implementation of three-dimensional Gibbs point processes with inhomogeneous and anisotropic pair-potential functions was the most important mathematical contribution, as only two-dimensional isotropic or geometric anisotropic models and methods have been available so far - to our knowledge. Furthermore, a new spatial statistical summary function was suggested for the cluster size analysis on different length scales in aggregated structures. The spatial statistical methods introduced in this work can be used for point processes in general and are important contributions to the point process literature.

There are three main contributions for applications. First, material specific image analysis routines were developed including a spatial pore space analysis methodology applicable to various porous materials. Working with the pore skeleton opens up possibilities to answer many research questions on pore connectivity and anisotropy. The analysis can be extended to study pore channel length and bottle neck distributions. Second, it was shown that some information on the three-dimensional material structure can be extracted from two-dimensional images. Consequently, the developed characterization from two-dimensional images enables efficient screening of material properties since two-dimensional images are often easier to obtain, especially with high resolution. Third, it was demonstrated how statistical models fitted to data from static images can be used to draw conclusions on dynamic chemical physical processes like colloidal particle aggregation and polymer phase separation.

The presented methodology is not limited to silica particle gels and polymer blended films, but can be applied to various other materials like fiber structures or foams. Three-dimensional models can be validated by comparing mass transport simulations through generated structures and experimentally obtained measurements. Such simulation studies can help to understand and control mass transport properties and function of the studied material. In that way, this work contributes to the development of the next generation sustainable materials by using predictive science to reduce the number of experiments based on valuable resources.

Bibliography

Atherton, T. J. and Kerbyson, D. (1999). Size invariant circle detection. *Image and Vision Computing*, 17:795–803. doi: 10.1016/S0262-8856(98)00160-7.

Baddeley, A. J. and Gill, R. D. (1997). Kaplan-Meier estimators of interpoint distance distributions for spatial point processes. *The Annals of Statistics*, 25 (1):263–292.

Baddeley, A. J. and Turner, R. (2000). Practical Maximum Pseudolikelihood for Spatial Point Patterns (with Discussion). *Australian & New Zealand Journal of Statistics*, 42 (3):283–322. doi: 10.1111/1467-9574.00144.

Baddeley, A. J., Coeurjolly, J. F., Rubak, E., and Waagepetersen, R. (2014). Logistic regression for spatial Gibbs point processes. *Biometrika*, 101 (2):377–392. doi: 10.1093/biomet/ast060.

Besag, J. E. (1975). Statistical analysis of non-lattice data. *The Statistician*, 24: 179–195.

Chiu, S. N., Stoyan, D., Kendall, W. S., and Mecke, J. (2013). *Stochastic Geometry and its Applications*. John Wiley and Sons, Chichester, 3 edition.

Couprie, M., Coeurjolly, D., and Zrour, R. (2007). Discrete bisector function and Euclidean skeleton in 2D and 3D. *Image and Vision Computing*, 25 (10):1519–1698. doi: 10.1016/j.imavis.2006.06.020.

Cowie, J. M. G. and Arrighi, V. (2007). *Polymers: Chemistry and Physics of Modern Materials*. CRC press, Boca Raton, 3 edition.

Cussler, E. (1997). *Diffusion: Mass Transfer in Fluid Systems*. Cambridge University Press, Cambridge, 2 edition.

de Kruif, K. G., Hoffmann, M. a. M., van Marle, M. E., van Mil, P. J. J. M., Roefs, S. P. F. M., Verheul, M., and Zoon, N. (1995). Gelation of proteins from milk. *Faraday Discussions*, 101 (1):185. doi: 10.1039/fd9950100185.

Deutch, J. M. and Oppenheim, I. (1987). The lennard-jones lecture. the concept of brownian motion in modern statistical mechanics. *Faraday Discussions of the Chemical Society*, 83:1–20. doi: 10.1039/DC9878300001.

Diggle, P. J. (2014). *Statistical analysis of spatial and spatio-temporal point patterns*. CRC Press, Taylor & Francis Group, Boca Raton, 3 edition.

Diggle, P. J., Fiksel, T., Grabarnik, P., Ogata, Y., and Stoyan, T. M., D. (1994). On Parameter Estimation for Pairwise Interaction Point Processes. *International Statistical Review*, 62 (1):99–117.

Einstein, A. (1905). Über die von der molekularkinetischen Theorie der Wärme geforderte Bewegung von in ruhenden Flüssigkeiten suspendierten Teilchen. *Annalen der Physik*, 322 (8):549–560. doi: 10.1002/andp.19053220806.

Evans, D. F. and Wennerström, H. (1994). *The colloidal domain, where Physics, Chemistry, Biology, and Technology meet*. VCH Publishers, Inc., New York.

Geyer, C. J. and Thompson, E. A. (1992). Constrained monte carlo maximum likelihood for dependent data. *Journal of the Royal Statistical Society. Series B (Methodological)*, 54 (3):657–699.

Giacomelli, C., Daniele, S., and Martini, C. (2017). Potential biomarkers and novel pharmacological targets in protein aggregation-related neurodegenerative diseases. *Biochemical Pharmacology*, 131:1–15. doi: 10.1016/j.bcp.2017.01.017.

Gibbs, J. W. (1902). *Elementary Principles in Statistical Mechanics*. Charles Scribner's Sons, New York.

Glasbey, C. A. and Horgan, G. W. (1995). *Image Analysis for the Biological Sciences*. John Wiley and Sons, Ltd, Chichester.

Grimmett, G. and Stirzaker, D. (2001). *Probability and Random Processes*. Oxford University Press, Oxford, 3 edition.

Hamngren Blomqvist, C., Gebäck, T., Altskär, A., Hermansson, A. M., Gustafsson, S., Lorén, N., and Olsson, E. (2016). Interconnectivity imaged in three dimensions: nano-particulate silica-hydrogel structure revealed using electron tomography. *In manuscript*.

Hawkes, P. W. *Electron Tomography: Methods for Three-Dimensional Visualization of Structures in the Cell*, chapter The electron microscope as a structure projector, pages 83–112. Springer, New York, 2 edition, (2006).

Heikkinen, J. and Penttinen, A. (1999). Bayesian Smoothing in the Estimation of the Pair Potential Function of Gibbs Point Processes. *Bernoulli*, 5 (6):1119–1136.

Illian, J., Penttinen, A., Stoyan, H., and Stoyan, D. (2008). *Statistical Analysis and Modelling of Spatial Point Patterns*. John Wiley & Sons, Chichester.

Israelachvili. (2011). *Intermolecular and Surface Forces*. Elsevier Inc., Burlington, 3 edition.

Jones, R. A. L. and Richards, R. W. (1999). *Polymers at Surfaces and Interfaces*. Cambridge University press, Cambridge.

Kendall, W. S. and Møller, J. (2000). Perfect simulation using dominating processes on ordered spaces, with application to locally stable point processes. *Advances in Applied Probability*, 32 (3):844–865.

Khan, M. N., Auerbach, S. M., and Monson, P. A. (2014). Lattice model for silica polymerization: Monte Carlo simulations of the transition between gel and nanoparticle phases. *The Journal of Physical Chemistry. B*, 118 (37):10989–99. doi: 10.1021/jp504961q.

Klemm, D., Heublein, B., Fink, H. P., and Bohn, A. (2005). Cellulose: Fascinating Biopolymer and Sustainable Raw material. *Angewandte Chemie International Edition*, 44:3358–3393. doi: 10.1002/anie.200460587.

Kolb, M. and Jullien, R. (1984). Chemically limited versus diffusion limited aggregation. *Journal de Physique Letttres*, 45 (20):977–981. doi: 10.1051/jphyslet:019840045020097700.

Marucci, M., Hjärtstram, J., Ragnarsson, G., Iselau, F., and Axelsson, A. (2009). Coated formulations: New insights into the release mechanism and changes in the film properties with a novel release cell. *Journal of Controlled Release*, 136:206–212. doi: 10.1016/j.jconrel.2009.02.017.

Marucci, M., Arnehed, J., Jarke, A., Matic, H., Nicholas, M., Boissier, C., and von Corswant, C. (2013). Effect of the manufacturing conditions on the structure and permeability of polymer films intended for coating undergoing phase separation. *European Journal of Pharmaceutics and Biopharmaceutics*, 83 (2):301–306. doi: 10.1016/j.ejpb.2012.09.020.

Mateu, J. and Montes, F. (2001). Likelihood Inference for Gibbs Processes in the Analysis of Spatial Point Patterns. *International Statistical Review*, 69 (1):81–104. doi: 10.2307/1403531.

Meakin, P. (1983). Formation of Fractal Clusters and Networks by Irreversible Diffusion-Limited Aggregation. *Physical Review Letters*, 51 (13):1119–1122.

Møller, J. (1999). Markov chain Monte Carlo and spatial point processes. In *Stochastic Geometry: Likelihood and Computation*, pages 141–172. Chapman & Hall/CRC, Boca Raton.

Møller, J. and Waagepetersen, R. P. (2004). *Statistical Inference and Simulation for Spatial Point Processes*. Chapman & Hall/CRC, Boca Raton.

Nordström, J., Matic, A., Sun, J., Forsyth, M., and MacFarlane, D. R. (2010). Aggregation, ageing and transport properties of surface modified fumed silica dispersions. *Soft Matter*, 6:2293–2299. doi: 10.1039/B921488G.

Ogata, Y. and Tanemura, M. (1981). Estimation of interaction potentials of spatial point patterns through the maximum likelihood procedure. *Annals of the Institute of Statistical Mathematics*, 33 (1):315–338. doi: 10.1007/BF02480944.

Otsu, N. (1979). A Threshold Selection Method from Gray-Level Histograms. *IEEE Transactions on Systems, Man, and Cybernetics*, 9 (1):62–66. doi: 10.1109/TSMC.1979.4310076.

Pennycook, S. J., Lupini, A. R., Varela, M., Borisevich, A. Y., Peng, Y., Oxley, M. P., and Chisholm, M. F. *Scanning microscopy for nanotechnology: techniques and applications*, chapter Scanning transmission electron microscopy for nanostructure characterization, pages 152–191. Springer, New York, (2006).

Penrose, M. (2003). *Random Geometric Graphs*. Oxford University Press, Oxford.

Penttinen, A. (1984). Modelling interaction in spatial point patterns: parameter estimation by the maximum likelihood method. *Jyväskylä Studies in Computer Science, Economics and Statistics*, 7. doi: 10.1007/s10182-009-0106-5.

Qui, Y. and Zhang, G. (2000). Research and Development Aspects of Oral Controlled-Release Dosage Forms. In *Handbook of Pharmaceutical Controlled Release Technology*, pages 465–504. Marcel Dekker, Inc., New York.

Rajala, T. (2010). Spatial point processes and graph based statistical features. *2000 Mathematics Subject Classification*, Preprint 385.

Ripley, B. D. and Kelly, F. P. (1977). Markov point processes. *Journal of the London Mathematical Society*, 15 (2):188–192.

Ruelle, D. (1969). *Statistical mechanics. Rigorous results*. Benjamin, New York.

Sakellariou, P. and Rowe, R. C. (1995). Interactions in cellulose derivative oral drug delivery. *Progress in Polymer Science*, 20:889–942. doi: 10.1016/0079-6700(95)00008-4.

Schladitz, K. and Baddeley, A. J. (2000). A Third Order Point Process Characteristic. *Scandinavian Journal of Statistics*, 27 (4):657–671. doi: 10.1111/1467-9469.00214.

Siegel, R. A. (2012). Porous Systems. In *Fundamentals and Applications of Controlled Release Drug Delivery*, pages 29–251. Springer, New York.

Siepmann, F., Siepmann, J., Walther, M., MacRae, R. J., and Bodmeier, R. (2008). Polymer blends for controlled release coatings. *Journal of Controlled Release*, 125 (1):1–15. doi: 10.1016/j.jconrel.2007.09.012.

Stelzer, H. K. *Handbook of Biological Confocal Microscopy*, chapter The intermediate optical system of laser-scanning confocal microscopes, pages 93–103. Plenum Press, New York, 2 edition, (1990).

Takacs, R. (1986). Estimator for the pair-potential of a gibbsian point process. *Statistics*, 17 (3):429–433. doi: 10.1080/02331888608801956.

Wang, J. and Sun, W. (2014). Heat and sweat transport in fibrous media with radiation. *European Journal of Applied Mathematics*, 25 (3):307–327. doi: 10.1017/S0956792514000059.

Wen, H. and Li, J. X. (2010). Introduction and overview of oral controlled release formulation design. In *Oral Controlled Release Formulation Design and Drug Delivery: Theory to Practice*, pages 1–19. John Wiley & Sons, Hoboken.

Yadav, S., Illa, M. P., Rastogi, T., and Sharma, C. S. (2016). High absorbency cellulose acetate electrospun nanofibers for feminine hygiene application. *Applied Materials Today*, 4:62 – 70. doi: 10.1016/j.apmt.2016.07.002.

Yuan, Y., Reece, T. J., Sharma, P., Poddar, S., Ducharme, S., Gruverman, A., Yang, Y., and Huang, J. (2011). Efficiency enhancement in organic solar cells with ferroelectric polymers. *Nature Materials*, 10:296–302. doi: 10.1038/nmat2951.